Originally published as:

Schneider, F. M., Yuan, X., Schurr, B., Mechie, J., Sippl, C., Haberland, C., Minaev, V., Oimahmadov, I., Gadoev, M., Radjabov, N., Abdybachaev, U., Orunbaev, S., Negmatullaev, S., GIPP (2013): Seismic imaging of subducting continental lower crust beneath the Pamir. - Earth and Planetary Science Letters, 375, 1, 101-112

DOI: 10.1016/j.epsl.2013.05.015

Graphical Abstract

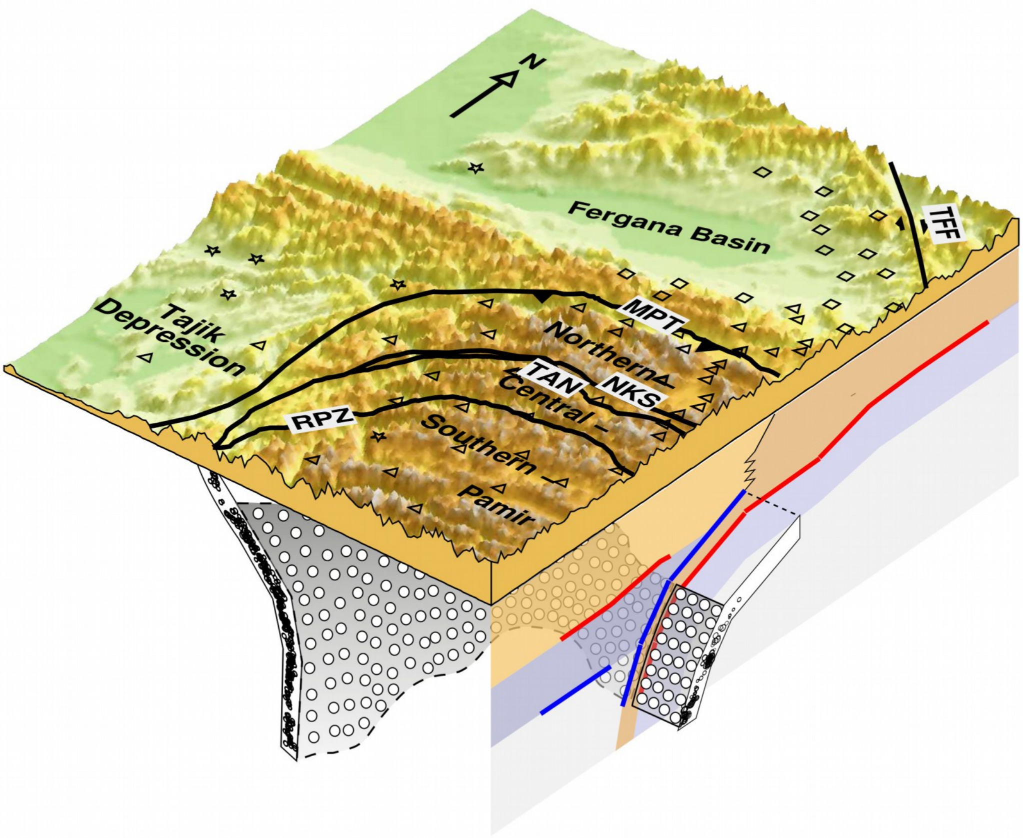

Highlights

We operated a modern seismic array in the Pamir, a key area for Indo-Asian collision.

We constructed receiver function cross sections traversing Tien Shan and Pamir.

We used a modified CCP stacking to image strongly dipping interfaces.

We observed subduction of Eurasian continental crust beneath the Pamir.

A south-dipping low-velocity zone coincides with the intermediate-depth seismicity.

Seismic imaging of subducting continental lower crust beneath the Pamir

F. M. Schneider [a,*], X. Yuan [a,*], B. Schurr [a], J. Mechie [a], C. Sippl [a], C. Haberland [a], V. Minaev [b], I. Oimahmadov [b], M. Gadoev [b], N. Radjabov [b], U. Abdybachaev [c], S. Orunbaev [c] and S. Negmatullaev [d]

[a] Deutsches GeoForschungsZentrum GFZ, Telegrafenberg, 14473, Potsdam, Germany

[b] Institute of Geology, Earthquake Engineering and Seismology, Academy of Sciences of the Republic of Tajikistan, Dushanbe 734063, Tajikistan

[c] Central Asian Institute for Applied Geosciences, 720027 Bishkek, Kyrgyzstan

[d] PMP International, 59 Shevchenko St., Dushanbe 734025, Tajikistan

* Corresponding authors. *E-mail address:* felix.schneider@gfz-potsdam.de or yuan@gfz-potsdam.de

A B S T R A C T

Exhumation of ultra-high pressure metamorphic rocks testifies that the continental crust can subduct to significant depth into the mantle despite its buoyancy. However, direct observation of ongoing subduction of continental crust is rare. The Pamir is regarded as a possible place of active continental subduction because of the intermediate-depth seismicity, crustal xenoliths and estimates of crustal shortening versus convergence rates. Here we present for the first time receiver function images from a passive-source seismic array traversing the Tien Shan and the Pamir plateau showing southward subduction of Eurasian continental crust. In the eastern Pamir, we

observe a southerly dipping 10-15 km thick low-velocity zone (LVZ) that extends from 50 km depth near the base of the crust to more than 150 km depth with a dip angle increasing to subvertical. While the upper- and mid- crustal material seems to be shortened and incorporated into the Pamir, the lower Eurasian crust detaches and subducts. In its deeper part (> 80 km) the LVZ envelopes the intermediate-depth earthquakes. Our observations imply that the complete arcuate intermediate depth seismic zone beneath the Pamir traces a slab of subducting Eurasian continental lower crust.

1. Introduction

The Pamir, situated north of the western Himalayan syntaxis, is thought to consist of the same collage of continental terranes as Tibet, that were progressively accreted to Eurasia prior to the Indian-Eurasian collision around 50 million years ago (Schwab et al., 2004). To regard the Pamir as a place where subduction of continental crust may occur is motivated tectonically, since the correlation of the Pamir and Tibetan belts and sutures indicates that structures in the Pamir were translated northwards by around 300 km with respect to Tibet. Thereby the crust connecting the Tajik and Tarim basins disappeared (Burtman and Molnar, 1993; Robinson et al., 2004), leading to the hypothesis that the Eurasian continental lithosphere is subducted along the Pamir's deformation front, which is today formed by the Main Pamir Thrust (MPT) (Burtman and Molnar, 1993; Hamburger et al., 1992; Sobel et al., 2013). Today, 10-15 mm/year of concentrated shortening occurs across the MPT (Zubovich et al., 2010), which is about one third of the total present-day Indian-Eurasian convergence rate. In the Pamir, the total amount of crustal shortening that occurred during the Cenozoic is even higher than in Tibet, since a similar amount of total convergence has been accommodated over a much smaller distance. Considering the relation of present to pre-Cenozoic crustal thicknesses, these extremely high amounts of crustal shortening in the Pamir yield realistic scenarios that require crustal excess (Schmidt et al., 2011). Besides, an indication for subduction of continental crust in this region was given by Roecker (1982), who first observed a low-velocity zone in the upper mantle dipping north beneath the Hindu Kush by local earthquake tomography. The most striking observation indicating continental subduction in the Pamir-Hindu Kush region is the vigorous intermediate-depth seismicity occurring from 70 to 250 km depth in this intra-continental setting. In map view, this seismicity forms a narrow S-shaped band of approximately 450 km length from the Hindu Kush in northeastern Afghanistan to the eastern Pamir (Fig. 1). The hypocentres of these mantle earthquakes form two separated Wadati-Benioff zones, one beneath the Pamir and one beneath the Hindu Kush (Burtman and Molnar, 1993; Fan et al., 1994; Negredo et al., 2007; Pegler, and Das, 1998). N-S oriented cross sections reveal opposite dips for both zones. There is a long standing debate whether the geometry of the seismic zone results from a single originally northward dipping subduction interface, which was contorted and overturned under the eastern Pamir (Billington et al., 1977; Pegler, and Das, 1998; Pavlis and Das, 2000), or if it is the result of two subduction zones, one dipping to the north beneath the Hindu Kush and one dipping to the south beneath the Pamir (Burtman and Molnar, 1993; Chatelain et al., 1980; Fan et al., 1994; Negredo et al., 2007). Recent high resolution earthquake locations from the local TIPAGE network (see next paragraph) show the seismicity in the Pamir as a curviplanar arc dipping to the south in the eastern Pamir and bending to an eastward dipping direction beneath the south-western Pamir, while the separated seismic zone beneath the Hindu Kush is a more complex structure striking east-west and dipping subvertically north to north-west (Sippl et al., 2013).

2. TIPAGE seismic experiment

The seismic data analyzed here were collected by a temporary experiment operated from 2008 to 2010 (Fig. 1). The experiment is the seismological component of the multi-disciplinary **Ti**en Shan **Pa**mir **Ge**odynamic Program (TIPAGE) (Mechie et al., 2012) and ran in two configurations. In the first year, 24 broadband stations were installed in the eastern Pamir forming a 350 km long north-south linear array from southern Kyrgyzstan to the Tajik-Afghan border with an average station spacing of 15 km. Additionally, 8 broadband and 8 short period stations were distributed in an areal network covering the whole Pamir. In the second year the network geometry was changed. 17 stations from the eastern Pamir linear array were relocated to densify the areal network in order to achieve an equidistant mesh with a station spacing of approximately 40 km. The areal array helped to accurately locate the local earthquakes (Sippl et al., 2013). We also included 5 permanent stations in western Tajikistan, operated by PMP International, Dushanbe. In the present work we concentrate on the receiver function analysis along the linear array. The profile was prolonged northwards with 10 stations from the FERGANA seismic experiment, running from 2009 to 2010 in the Fergana Valley (Haberland et al., 2011).

3. Receiver function processing

The receiver function (RF) method is a widely used seismological tool to image crustal and upper mantle seismic discontinuities underneath seismic stations (Kind et al., 2012; Rondenay, 2009; Bostock, 2007). This technique identifies the discontinuities, e.g. the Moho, by detecting mode conversion from compressional (P) to shear (S) waves. The time delay between the converted wave (Ps) and the mother phase (P) determines the conversion depth. The amplitude and phase of the Ps conversions reflects the nature of the discontinuity, such as the sign, strength and sharpness of the velocity contrast. The kernel of the receiver function algorithm is composed of two main steps, a coordinate rotation that isolates the Ps converted waves from the P wave; and a deconvolution that removes the source-side complications and the propagation effects. Further processing steps such as moveout correction, common-conversion-point (CCP) stack and migration enable the construction of station stack averages and receiver function profiles for dense seismic arrays (Bostock et al., 2001; Kind et al., 2002; Yuan et al., 1997). There are different flavors in RF processing in terms of coordinate rotation and deconvolution. Here we calculate receiver functions in the manner described by Yuan et al. (1997). We used high quality teleseismic earthquake records originating at epicentral distances between 30° and 90° (Fig. 1). All records were bandpass filtered (0.5-30 s). For event selection records of all events with magnitudes bigger than 5.5 were inspected manually. If needed, additional high pass filters (20 s ,15 s ,10 s ,7.5 s or 5 s) were applied. We rotate the originally recorded Z-N-E components to the L-Q-T coordinate system using theoretical back azimuths and incidence angles and deconvolve the L component from the Q and T components by a time-domain Wiener filtering approach. The Q and T components correspond to the polarizations of the SV and SH component, respectively. The deconvolved Q and T components are called Q- and T- receiver functions (QRF and TRF). For horizontally layered isotropic media the Ps converted waves are polarized in the radial direction and can be analyzed by the QRF. In the case of dipping interfaces or anisotropy significant converted energy will fall in the transverse direction and can be detected by the TRF. Using the obtained RFs, we then create a receiver function depth section (Fig. 2) by a CCP stack approach (Kind et al., 2002). The approach divides the depth section into a fine grid and stacks at each grid cell those samples of the receiver functions that have originated by Ps conversion in the same grid cell. The conversion points are calculated by ray tracing through a reference velocity model.

4. Depth sections along the N-S profile

4.1 CCP stacking for horizontal converters

Figure 2 shows the CCP cross section constructed along the north-south directed linear array. Beneath the Pamir we observe an ~70 km thick crust, whereas in the north towards the Fergana Valley crustal thickness decreases rapidly to ~45 km beneath the northern edge of the southern Tien Shan. A prominent southward dipping structure is evident in the uppermost mantle south of the MPT. The dipping structure consists of two parallel phases with a negative phase above and a positive phase below. The two phases define a low velocity zone (LVZ) that dips towards the south, slightly offset from the deep seismicity in this cross section. However, since the CCP section assumes horizontally layered discontinuities, strongly dipping structures are not properly reconstructed. They tend to shift to shallower positions.

4.2 CCP stacking for dipping layers

The CCP stack using a horizontally layered (1D) reference model remains valid if the object to be reconstructed is horizontal or slightly inclined. If mode conversion occurs on strongly dipping interfaces, the corresponding ray paths differ significantly from ray paths that belong to mode conversions at horizontally oriented interfaces (Fig. 3). Thus the locations of the conversion points from inclined structures are not properly calculated if a horizontally layered earth is assumed. In order to reconstruct inclined structures we calculate ray paths that satisfy Snell’s law at a converter with an assumed inclination angle. This method was already applied by Li et al. (2000) and Kawakatsu and Watada (2007).

4.2.1 Synthetic tests

Strongly inclined interfaces can only be properly reconstructed by taking into account the corresponding inclination in the migration. We conducted synthetic experiments to test the CCP stack of receiver functions assuming horizontal and dipping converters. We used the RAYSUM (Frederiksen and Bostock, 2000) code to compute QRF and TRF for models involving a horizontal Moho and a dipping low-velocity zone (LVZ) with dip angles of 30°, 45° and 65°, respectively (Fig. 4). The dipping LVZ produces a double phase with the negative one above and the positive one below, marked by black lines in each figure. The structures are reconstructed by CCP stacking of QRF and TRF assuming horizontal and dipping converters, respectively. In the QRF, both the Moho and the LVZ are visible, whereas in the TRF only the dipping LVZ is present. For both QRF and TRF, an aberration in the reconstruction of the dipping slab phase assuming horizontal converters already exists for a 30° dip and increases with increasing dip angle.

Assuming horizontal converters, the dipping interface tends to be shifted to a shallower position. The dipping phases have been properly reconstructed by assuming dipping converters with corresponding dips. Interestingly, a strongly dipping interface changes its polarity in the QRF, which may reduce the coherence in the CCP stack section. On the transverse (T) component (TRF) the inclined interfaces produce significant or even clearer signals than on the QRF (Abe et al., 2011) (Fig. 4). Here, only events from azimuths between 0° and 180° for a south-dipping LVZ are plotted. Events with azimuths between 180° and 360° would show reversed polarity for the TRF.

4.2.2 QRF and TRF cross sections assuming inclined converters

Fig. 5 shows migrated QRFs and TRFs assuming converting interfaces dipping 65° to the south. The QRF section (Fig. 5a) shows that by assuming inclined converters the dipping structure is migrated to the proper position which coincides with the deep seismicity. The TRF section (Fig. 5b) is dominated by the dipping structure, since horizontal converters such as the Moho do not produce signals on the T-component. The double phase in the TRF section connects the intermediate depth seismicity to the base of the crust just below and south of the MPT. It provides clear evidence for a southward subduction configuration for the eastern Pamir. Tectonic models for the Pamir-Hindu-Kush seismic zone with a single originally north-dipping overturned slab of Indian provenance should thus be discarded.

4.2.3 Reconstruction of the dipping low-velocity zone

The migration shown in Fig. 5 is strictly only valid for structures with an inclination angle of about 65°. Interfaces with other dips are shifted to wrong positions. Figure 6 shows the CCP stacks of QRF and TRF along the linear array assuming different inclination angles ranging from 0° (horizontally layered) to 65°. From each image the corresponding information is picked and displayed in the right column. The summation of all images is displayed in the bottom figure. The resulting image shows two parallel running phases, the upper one with negative and the lower one with positive amplitude dipping to the south. The inclination angles increase with depth from 30° around the Moho to 65° around 150 km depth. Circles mark the locations of the earthquake hypocenters occurring between 73° and 75°E that have been recorded and located by our network (Sippl et al., 2013). The dipping structure coincides with the location of the Wadati-Benioff zone indicated by the hypocenters. The signs of the imaged velocity contrasts (velocity decrease followed by velocity increase) indicate the existence of a low-velocity zone (LVZ) between the phases.

4.3 Combined 2D - model from CCP depth sections

Figure 7a shows the entire 2D model along the N-S profile obtained from the information displayed in Fig. 2 and 6. It summarizes the RF results from CCP stacking along the N-S profile. They show the crustal thicknesses as discussed in section 4.1 and the LVZ connected to the Eurasian lower crust south of the MPT. In this reconstruction, that takes into account the raypaths of converted waves from the inclined conversion layers of the LVZ, the intermediate depth earthquakes are located within its borders. Since CCP stacking results tend to overestimate the thickness of the LVZ due to lateral smoothing, we perform forward modeling of its phases to estimate its thickness and velocity contrast in the following section 6. The red plane in Fig. 7b shows the position of the N-S cross section relative to the intermediate depth seismic zone at its eastern end. The green plane shows the position of a subsidiary depth section constructed from our data, that is discussed in the next section.

5 Depth section in NW-SE direction

Subsidiary to depth sections along the main TIPAGE profile, an additional cross section is constructed in the northwest to southeast direction using the areally distributed stations of the TIPAGE network (Fig. 8). The orientation is chosen perpendicular to the strike of the intermediate depth seismic zone (see green line in Fig. 1 and green plane in Fig. 7b).

Although the resolution of the additional cross section is, due to the sparser station distribution, not as good as that of the N-S cross section along the main profile, a very similar configuration as in the main section can be identified. The QRF section shows a 70 km thick crust in the southeast that shallows towards the northwest (Fig. 8a). A southeast dipping structure is evident starting at ~38° N. Figure 8b shows the TRF section that is migrated assuming inclined converters (see section 4.2). As in the north-south cross section, the TRFs show coherent negative and positive dipping phases coinciding with the earthquake hypocenters. It connects the intermediate depth seismicity to the lower crust in the north-west. It is likely that the observed structure is the same as in the north-south profile, but rotated anticlockwise by 45°.

6 Forward modeling

The basic characteristics of the double phase imaging the LVZ are determined by forward modeling. An example of the comparison between observed and synthetic receiver functions at station P18, located in the southern part of the linear array (P18), imaging the LVZ at around 100 km depth is given in Fig. 9. By modeling the double phase we obtained a thickness of the low velocity zone of 10.5 +/- 1 km at station P18. At five further stations in the vicinity of P18, the LVZ phases could be identified in the TRFs with back azimuths ranging from 30° to 110°. The LVZ thickness appears to vary laterally between 10 and 15 km (see Figs. S4, S5 and S6 in the Supplementary material for estimation of error and lateral variation). Amplitude modeling of the Moho Ps phase in the QRFs and the double phase in the TRFs, reveals the velocity contrast between the LVZ and the surrounding mantle at 100 km depth to be only slightly smaller compared to the velocity contrast at the Moho ($\Delta v_{LVZ} = 0.97\Delta v_{Moho}$), implying that the velocity in the LVZ is very similar to the velocity of the lower crust (Fig. 10)

6.1 Comparison of modeled and observed RFs for the entire azimuth range

Figs. 9a and 9c show all the individual QRF- and TRF- traces of station P18, sorted by back azimuth. The summation traces are shown in the upper panels. In the QRF the Moho at ~8 s is the dominant phase. The double slab phase with negative-positive polarities is clearly seen at

10-15 s in the TRF, and can also be recognized in the individual QRF traces. We calculated the synthetic QRF (Fig. 9b) and TRF (Fig. 9d) with the RAYSUM code (Frederiksen and Bostock, 2000) using a simple three layered regional model, including a 10.5 km thick LVZ that dips to the south at an angle of 50° and a 65 km thick crust with a flat Moho (illustrated by the black lines in Figures 9e-9h). The values of slownesses and back azimuths for the synthetic RFs were chosen identical to those of the observed RFs. The majority of the RFs have back azimuths of 0-180°. Few events come from the west (see Fig. 1). Furthermore, the same post-processing as for the observed data (low pass filter and deconvolution) is applied to the synthetics.

Moho conversions are observed in the QRFs at 8s. The first multiple phase (PpPs) of the Moho (at ~29 s) is very (to the point of being invisible) weak in the observed RFs due to noise, lateral heterogeneity or a crust-mantle transition gradient. Surprisingly, the second multiple (PpSs) is clearly visible, though at reduced amplitude.

The primary phases of the dipping layers are well matched by both the synthetic QRFs and TRFs between 10 s at 0° azimuth and 16 s at 180° azimuth. Although too few TRFs from western backazimuths (σ) are available to verify the polarity flip of the inclined phase seen in the synthetics, there are sufficient RFs recorded that show both quadrants in the east to have the same polarity, ruling out anisotropy, which would show a 2σ symmetry. Thus, the waveform modeling verifies the existence of a dipping LVZ. Fig. 9e-9h shows the comparison of the CCP stack of QRFs and TRFs assuming converters inclined at an angle of 50°. The amplitude of the QRFs changes its sign on the inclined interface, which may explain the reduced coherence of the reconstructed dipping phase in the QRFs compared to the TRFs.

6.2 Waveform modeling for thickness and velocity contrast of the low velocity zone

Modeling waveforms of the slab phases can provide information on the velocity of the LVZ. However, due to diverse sources of noise, lateral heterogeneity, anisotropy and data processing, amplitudes of receiver function summations often underestimate the true velocity contrast. These effects should be similar for the slab and the Moho phases. In Fig. 10 we compare modeled amplitudes of the slab phase with that of the Moho conversion for station P18. We consider the most coherent part of the receiver functions in the azimuthal range of 100-110° in order to reduce noise and heterogeneity. We stack QRFs and TRFs and extract the Moho Ps phase from the QRFs and the slab Ps phase from the TRFs. Synthetic QRFs and TRFs are modeled for the same azimuth and slowness values and treated in the same way as the observed data. The summation traces of synthetic and observed seismograms are compared. First, the amplitudes of the data are normalized to fit the velocity contrast (Δv_m) of Vs from 4.6 km/s to 4.15 km/s at the Moho (Mechie et al., 2012). The velocity contrast between the LVZ and the mantle is chosen relative to $\Delta v_{m.}$. At station P18, the best fit between modeled and observed amplitudes of the slab Ps phase is achieved for a 10.5 km thick LVZ with a velocity contrast of 0.97 Δv_m, implying that the velocity of the LVZ is very similar to that of the lower crust. Assuming an S-wave velocity (Vs) of 4.6 km/s in the upper mantle, we obtain a Vs of 4.16 km/s in the LVZ. Thus we conclude that the LVZ is composed of lower-crustal material.

7 Crustal thickness in the Pre-Cenozoic

The initial crustal thickness of the Pamir prior to the Cenozoic deformation is crucial to understand its evolution (Schmidt et al., 2011). The thickness of pre-deformed Pamir crust may be best estimated by examining the crustal thicknesses of the flat basin areas surrounding the Pamir. Controlled-source seismic profiling revealed a crustal thickness of 45-50 km in the central Tarim basin (Li et al., 2006). A similar estimate of the crustal thickness beneath the eastern Fergana basin can be obtained by our receiver function profile (Fig. 2). Here, we analyze receiver functions of stations (SHAA, IGRN and FRK9) in the central part of the Tajik basin, that yield a crustal thickness of ~45 km.

7.1 Crustal thickness in the Tajik basin

The crustal thickness of the Tajik basin is determined using the depth - Vp/Vs slant stacking technique (Zhu and Kanamori, 2000) at the stations SHAA, IGRN and FRK9 (see Fig. 1 for their location). Receiver functions are often complicated for stations located in basins due to strong multiple reverberations in the sediments (Zheng et al., 2005). In order to suppress these inner crustal phases the data are low pass filtered with a corner frequency of 2 seconds. In Fig. 11, for each of these stations the slant stacking results show crustal thicknesses larger than 45 km (left column). The right column shows the corresponding receiver functions sorted by slowness (lower panels) and the summation traces moveout-corrected for the Ps, PpPs and PpSs phases (as labeled, upper panels). The theoretical arrival times of the Ps, PpPs and PpSs phases, calculated from the depth and Vp/Vs values of the slant stack result, are marked by black, yellow and blue lines respectively. Direct Moho conversions and their multiples can be distinguished due to the reversed moveout of the multiples. For all stations the Moho Ps conversion (at around 8 s) is supported by the PpPs and PpSs phases at around 19 s and 25 s. The observed Vp/Vs values of 1.78, 1.81 and 1.86 at stations SHAA, FRK9 and IGRN are in a realistic range but higher than the global average, probably due to the very thick sedimentary cover in the Tajik Depression (Nikolaev, 2002).

8 Discussion

While low velocity layers hosting earthquakes at intermediate depths in subduction settings are a common feature in oceanic subduction zones (Bostock, 2012; Ferris et al., 2003), they are rare in intra-continental collisional settings. Moreover, we think that the material we observe as the LVZ is of continental origin, since the LVZ is clearly connected to the overlying Eurasian lower crust (Fig. 5) and subduction of oceanic material should have stopped with the final closure of the Tethys ocean no later than 40 million years ago (Yin and Harrison, 2000). The absence of Cenozoic volcanism (Schwab et al., 2004) supports this interpretation. Besides, findings of crustal xenoliths of clearly Eurasian provenance in the south-eastern Pamir testify that crustal rocks have resided at least at 90 km depth in this region (Hacker et al., 2005). Together with our observation of the south-dipping LVZ this provides strong evidence for ongoing subduction of Eurasian continental crust beneath the Pamir (Fig. 7a). The crustal thicknesses of the surrounding basins of the Pamir can be regarded as a proxy for the pre-Cenozoic crustal thickness of the Pamir, as the basins are thought to have been stable during the Cenozoic convergence. Since we observed crustal thicknesses of more than 45 km in the Fergana and Tajik Basin (Fig 2 and 11) and similar crustal thicknesses have been observed for the Tarim Basin (Li et al., 2006) it appears reasonable to assume a similar pre-Cenozoic crustal thickness of at least 40 km in the Pamir. Estimation of the budget of crustal shortening during the Cenozoic Indian-Eurasian convergence suggests that, based on this initial crustal thickness, a significant amount of continental crust must have been lost, most likely having been recycled into the mantle (Schmidt et al., 2011), which is consistent with our observations. In contrast to previous models of continental subduction in the Pamir that inferred the subduction of intact albeit thinned crust (Burtman and Molnar, 1993), our observation suggests that only the lower part of the crust subducts (Fig. 7a). Upper and mid-crustal Eurasian material is underthrusted and incorporated into the Pamir. While the upper crust undergoes brittle deformation reflected by crustal seismicity in the upper 30 km, the mechanically weakened mid-crustal material (dashed region in Fig. 7a) is ductilely shortened and decoupled from the lower crust. Although the buoyancy of the continental crust tends to prevent it from being subducted into the mantle, the outcrops of ultra-high pressure metamorphic rocks suggest that continental crust can exist deep in the mantle (Chopin, 1984; Hacker et al., 2006; Okay et al., 1989). Due to crustal thickening in continental collision zones lower crust can reach pressures where it transforms to denser eclogite, which reverses the buoyancy and hence may drive its subduction (Molnar and Gray, 1979; Krystopowicz and Currie, 2013). The seismic velocity contrast between crust and mantle should then be decreased through eclogitization (Gubbins et al., 1994), which is supported by our observation of the decreasing intensity of the velocity contrasts of the LVZ below 100 km depth in the migrated cross sections (Figs. 5 and 6). Since fully eclogitized crustal material would be seismically invisible our observation suggests that eclogitization has not been completed above 150 km depth.

The occurrence of the intermediate-depth earthquakes inside the LVZ implies that these earthquakes are caused by processes in the subducted crust, which may be attributed to dehydration embrittlement (Kirby et al., 1996) or shear instability (John et al., 2009; Kelemen and Hirth, 2007). The most recent study of the Pamir – Hindu Kush seismicity reveals an arc-like geometry of the seismic zone beneath the Pamir (Sippl et al., 2013) (Fig. 7b). It is resolved as a relatively smoothly connected layer with a dip direction changing from eastwards to southwards from its southwestern to its eastern end. Our observation that the earthquakes occur within the crust at the eastern end and assuming the same petrological mechanisms enable seismicity within the whole arc, implies that the complete arc is of crustal material. In the subsidiary NW-SE cross section (Fig. 8), constructed using the stations of the areally distributed stations of the TIPAGE network and crossing the intermediate depth seismic zone perpendicularly about 130 km to the west, a dipping LVZ can also be recognized in the TRF section (Fig. 8b), connecting the intermediate depth seismic zone to the lower crust. This additional observation supports our conclusion, that the arc described by the earthquake hypocentres traces a slab of Eurasian continental lower crust that subducts beneath the Pamir.

Acknowledgments

This work was supported by the Deutsche Forschungsgemeinschaft and by the Deutsches GeoForschungsZentrum Potsdam. Seismic stations were provided by the Geophysical Instrument Pool Potsdam. Waveform data are archived at the GEOFON data center. We are grateful to all field team members of both the TIPAGE and FERGANA experiments. We would like to thank Frederik Tilmann for comments and discussions.as well as Hitoshi Kawakatsu and one anonymous referee for their useful suggestions for the manuscript. We used Seismic Handler (Stammler, 1993) for receiver function processing and GMT (Wessel and Smith, 1991) for production of the most figures.

Appendix A. Supplementary material

Supplementary material associated with this article can be found in the online version.

References

Abe, Y., Ohkura, T., Hirahara, K., Shibutani, T., 2011. Common conversion point stacking of receiver functions for estimating the geometry of dipping interfaces. Geophys. J. Int. 185, 1305–1311.

Billington, S., Isacks, B.L., Barazangi, M., 1977. Spatial distribution and focal mechanisms of mantle earthquakes in the Hindu Kush-Pamir region: A contorted Benioff zone. Geology 5, 699–704.

Bostock, M.G., 2007. Teleseismic Body-Wave Scattering and Receiver-Side Structure, in: Schubert, G. (Ed.), Treatise on Geophysics. Elsevier, Amsterdam, pp. 219–246.

Bostock, M.G., 2012. The Moho in subduction zones. Tectonophysics.

Bostock, M.G., Rondenay, S., Shragge, J., 2001. Multiparameter two-dimensional inversion of scattered teleseismic body waves 1. Theory for oblique incidence. J. Geophys. Res. 106, 30771–30782.

Burtman, V.S., Molnar, P., 1993. Geological and geophysical evidence for deep subduction of continental crust beneath the Pamir. Spec. Pap. Geol. Soc. Am. 281.

Chatelain, J.L., Roecker, S.W., Hatzfeld, D., Molnar, P., 1980. Microearthquake Seismicity and fault plane solutions in the Hindu Kush region and their tectonic implications. J. Geophys. Res. 85, 1365–1387.

Chopin, C., 1984. Coesite and pure pyrope in high-grade blueschists of the Western Alps: a first record and some consequences. Contrib. Mineral. Petr. 86, 107–118.

Fan, G., Ni, J.F., Wallace, T.C., 1994. Active tectonics of the Pamirs and Karakorum. J. Geophys. Res. 99, 7131–7160.

Ferris, A., Abers, G.A., Christensen, D.H., Veenstra, E., 2003. High resolution image of the subducted Pacific (?) plate beneath central Alaska, 50–150 km depth. Earth Planet. Sc.

Lett. 214, 575–588.

Frederiksen, A.W., Bostock, M.G., 2000. Modelling teleseismic waves in dipping anisotropic structures. Geophys. J. Int. 141, 401–412.

Gubbins, D., Barnicoat, A., Cann, J., 1994. Seismological constraints on the gabbro-eclogite transition in subducted oceanic crust. Earth and Planetary Science Letters 122, 89–101.

Haberland, C., Abdybachaev, U., Schurr, B., Wetzel, H.-U., Roessner, S., Sarnagoev, A., Orunbaev, S., Janssen, C., 2011. Landslides in southern Kyrgyzstan: Understanding tectonic controls. Eos Trans. AGU 92, PAGE 169.

Hacker, B., Luffi, P., Lutkov, V., Minaev, V.T., Ratschbacher, L., Plank, T., Ducea, M.N., Patino-Douce, A., McWilliams, M., Metcalf, J., 2005. Near-Ultrahigh Pressure Processing of Continental Crust: Miocene Crustal Xenoliths from the Pamir. J. Petrology 46, 1661–1687.

Hacker, B.R., Wallis, S.R., Ratschbacher, L., Grove, M., Gehrels, G., 2006. High-temperature geochronology constraints on the tectonic history and architecture of the ultrahigh-pressure Dabie-Sulu Orogen. Tectonics 25.

Hamburger, M.W., Sarewitz, D.R., Pavlis, T.L., Popandopulo, G.A., 1992. Structural and seismic evidence for intracontinental subduction in the Peter the First Range, Central Asia. Geol. Soc. Am. Bull. 104, 397–408.

John, T., Medvedev, S., Rüpke, L.H., Andersen, T.B., Podladchikov, Y.Y., Austrheim, H., 2009. Generation of intermediate-depth earthquakes by self-localizing thermal runaway. Nature Geosci. 2, 137–140.

Kawakatsu, H., Watada, S., 2007. Seismic Evidence for Deep-Water Transportation in the Mantle. Science 316, 1468 –1471.

Kelemen, P.B., Hirth, G., 2007. A periodic shear-heating mechanism for intermediate-depth earthquakes in the mantle. Nature 446, 787–790.

Kind, R., Yuan, X., Kumar, P., 2012. Seismic receiver functions and the lithosphere–asthenosphere boundary. Tectonophysics 536–537, 25–43.

Kind, R., Yuan, X., Saul, J., Nelson, D., Sobolev, S.V., Mechie, J., Zhao, W., Kosarev, G., Ni, J., Achauer, U., Jiang, M., 2002. Seismic Images of Crust and Upper Mantle Beneath Tibet: Evidence for Eurasian Plate Subduction. Science 298, 1219–1221.

Kirby, S., Engdahl, R.E., Denlinger, R., 1996. Intermediate-depth intraslab earthquakes and arc volcanism as physical expressions of crustal and uppermost mantle metamorphism in subducting slabs. Subduction Top to Bottom, Geophys. Monogr. Ser. 96, 195–214.

Krystopowicz, N.J., Currie, C.A., 2013. Crustal eclogitization and lithosphere delamination in orogens. Earth Planet. Sc. Lett. 361, 195–207.

Li, S., Mooney, W.D., Fan, J., 2006. Crustal structure of mainland China from deep seismic sounding data. Tectonophysics 420, 239–252.

Li, X., Sobolev, S.V., Kind, R., Yuan, X., Estabrook, C., 2000. A detailed receiver function image of the upper mantle discontinuities in the Japan subduction zone. Earth Planet. Sc. Lett. 183, 527–541.

Mechie, J., Yuan, X., Schurr, B., Schneider, F., Sippl, C., Ratschbacher, L., Minaev, V., Gadoev, M., Oimahmadov, I., Abdybachaev, U., Moldobekov, B., Orunbaev, S., Negmatullaev, S., 2012. Crustal and uppermost mantle velocity structure along a profile across the Pamir and southern Tien Shan as derived from project TIPAGE wide-angle seismic data. Geophys. J. Int. 188, 385–407.

Molnar, P., Gray, D., 1979. Subduction of continental lithosphere: Some constraints and uncertainties. Geology 7, 58 –62.

Negredo, A.M., Replumaz, A., Villaseñor, A., Guillot, S., 2007. Modeling the evolution of continental subduction processes in the Pamir–Hindu Kush region. Earth Planet. Sc. Lett. 259, 212–225.

Nikolaev, V.G., 2002. Afghan-Tajik depression: Architecture of sedimentary cover and evolution. Russian Journal of Earth Sciences 4, 399–421.

Okay, A.I., Shutong, X., Sengor, A.M.C., 1989. Coesite from the Dabie Shan eclogites, central China. Eur. J. Mineral. 1, 595–598.

Pavlis, G.L., Das, S., 2000. The Pamir-Hindu Kush seismic zone as a strain marker for flow in the upper mantle. Tectonics 19, 103–115.

Pegler,, G., Das, S., 1998. An enhanced image of the Pamir–Hindu Kush seismic zone from relocated earthquake hypocentres. Geophys. J. Int. 134, 573–595.

Robinson, A.C., Yin, A., Manning, C.E., Harrison, T.M., Zhang, S.-H., Wang, X.-F., 2004. Tectonic evolution of the northeastern Pamir: Constraints from the northern portion of the Cenozoic Kongur Shan extensional system, western China. Geol. Soc. Am. Bull. 116, 953–973.

Roecker, S.W., 1982. Velocity Structure of the Pamir-Hindu Kush region: possible evidence of subducted crust. J. Geophys. Res. 87, 945–959.

Rondenay, S., 2009. Upper Mantle Imaging with Array Recordings of Converted and Scattered Teleseismic Waves. Surv. Geophys. 30, 377–405.

Schmidt, J., Hacker, B.R., Ratschbacher, L., Stübner, K., Stearns, M., Kylander-Clark, A., Cottle, J.M., Alexander, A., Webb, G., Gehrels, G., Minaev, V., 2011. Cenozoic deep crust in the Pamir. Earth Planet. Sc. Lett. 312, 411–421.

Schwab, M., Ratschbacher, L., Siebel, W., McWilliams, M., Minaev, V., Lutkov, V., Chen, F., Stanek, K., Nelson, B., Frisch, W., Wooden, J.L., 2004. Assembly of the Pamirs: Age and origin of magmatic belts from the southern Tien Shan to the southern Pamirs and their relation to Tibet. Tectonics 23, 31 PP.

Sippl, C., Schurr, B., Yuan, X., Mechie, J., Schneider, F.M., Gadoev, M., Orunbaev, S., Oimahmadov, I., Haberland, C., Abdybachaev, U., Minaev, V., Negmatullaev, S., Radjabov, N., 2013. Geometry of the Pamir-Hindu Kush intermediate-depth earthquake zone from local seismic data. J. Geophys. Res., http://dx.doi.org/10.1002/jgrb.50128

Sobel, E.R., Chen, J., Schoenbohm, L.M., Thiede, R., Stockli, D.F., Sudo, M., Strecker, M.R., 2013. Oceanic-style subduction controls late Cenozoic deformation of the Northern Pamir orogen. Earth Planet. Sc. Lett. 363, 204–218.

Stammler, K., 1993. Seismichandler—Programmable multichannel data handler for interactive and automatic processing of seismological analyses. Computers & Geosciences 19, 135–140.

Wessel, P., Smith, W.H.F., 1991. Free software helps map and display data. Eos, Transactions American Geophysical Union 72, 441–446.

Yin, A., Harrison, T.M., 2000. Geologic Evolution of the Himalayan-Tibetan Orogen. Annu. Rev. Earth Pl. Sc. 28, 211–280.

Yuan, X., Ni, J., Kind, R., Mechie, J., Sandvol, E., 1997. Lithospheric and upper mantle structure of southern Tibet from a seismological passive source experiment. J. Geophys. Res. 102, 27491–27,500.

Zheng, T., Zhao, L., Chen, L., 2005. A detailed receiver function image of the sedimentary structure in the Bohai Bay Basin. Phys. Earth Planet. In. 152, 129–143.

Zhu, L.P., Kanamori, H., 2000. Moho depth variation in southern California from teleseismic receiver functions. J. Geophys. Res.-Sol. Ea. 105, 2969–2980.

Zubovich, A.V., Wang, X., Scherba, Y.G., Schelochkov, G.G., Reilinger, R., Reigber, C., Mosienko, O.I., Molnar, P., Michajljow, W., Makarov, V.I., Li, J., Kuzikov, S.I., Herring, T.A., Hamburger, M.W., Hager, B.H., Dang, Y., Bragin, V.D., Beisenbaev, R.T., 2010. GPS velocity field for the Tien Shan and surrounding regions. Tectonics 29, 23 PP.

Figure Captions

Figure 1. Map of the Pamir with locations of the seismic stations used in this study. Major tectonic features such as sutures and faults marked in the map are (from north to south): Talas Fergana fault (TFF), Main Pamir thrust (MPT), Northern Pamir / Kunlun Suture (NKS), Tanymas Suture (TAN), Rushan Pshart Zone (RPZ), and Shyok suture (SHY). Red and green highlighted stations were used for the construction of the N-S and the NW-SE depth sections, respectively. The blue highlighted stations are used to determine the crustal thickness in the Tajik depression (section 7.1). Insets show a map of teleseismic events used and a map of the Indian-Eurasian collision zone. The area of altitudes exceeding 3000m is highlighted in brown, showing the area of Tibet, Himalaya, Pamir and Tien Shan. The red and green lines denote the projection planes of the N-S (Figs. 2 and 5) and NW-SE (Fig. 8) cross sections, respectively.

Figure 2. Common conversion point (CCP) image of Q-component receiver functions (QRF) along the N-S main profile. Positive velocity contrasts such as the Moho are shown in red colors, negative velocity contrasts in blue colors. Dashed lines mark the Moho and the double phase of the subducting low velocity zone (LVZ). Black dots denote the intermediate-depth earthquakes located with our network (Sippl et al., 2013) within 45 km of the profile. After

CCP stacking a boxcar filter with 20 km diameter was applied. The data were amplified by a factor of 20. The inset shows the color scale of the RF- amplitudes. This figure is shown without interpretation lines in Fig. S1 in the Supplementary material. Key: see Fig. 1.

Figure 3. Ray geometry of P to S converted waves at horizontal vs. inclined discontinuities. In the case of a horizontal boundary (left) the conversion point is situated on the left side of the station. In contrast, the conversion point at the inclined structure (dip angle δ=45°) is located on the right side of the station. Incidence and conversion angles in this figure are calculated for a P-wave velocity of 8 km/s below and an S-wave velocity of 4.15 km/s above the discontinuity, as may be realistic for a discontinuity between lower-crustal material and the mantle.

Figure 4. Synthetic migration test for a single station assuming an inclined geometry of the slab. The discontinuities of the input model are depicted as black lines. The slab dips to the south (180°). Synthetics are calculated for events with a slowness of 6.4 s/° and backazimuths between 0° and 180° with an increment of 10°. Since the model is symmetric (2.5D), events from backazimuths between 180° to 360° and those from backazimuths between 0° and 180° would be identical for the QRFs, and would sum to zero for the TRFs.

Figure 5. Migrated CCP stack receiver function cross sections assuming 65° inclined conversion interfaces. Q-component and T-component RF are shown in (A) and (B), respectively. The same processing on the CCP stacked data was applied as in Fig. 2. This figure is shown without interpretation lines in Fig. S2 in the Supplementary material. Key: see Fig. 1.

Figure 6: Migrated cross sections along the TIPAGE main seismic profile assuming different inclination angles of the converters. The assumed angles are depicted on the left. In the left and middle columns the amplitudes of the Q- and T-components are shown, respectively. For the T-component only events from the east (azimuthal angles 0°-180°) are taken into account. In the right column the positions of the conversion boundaries corresponding to the relevant dip angle are highlighted in red (positive converters) and blue (negative converters). The bottom figure shows the amalgamation of all picked elements from the right columns.

Figure 7. A: Cartoon showing reconstruction of the crust and mantle lithosphere at the northern margin of the India (Pamir) – Eurasian collision zone based on the observations of this study. Positive velocity contrasts such as the Moho are shown in red colors, negative velocity contrasts in blue colors. Bold interfaces and events are taken from Figs. 2 and 6. The shaded region depicts a zone that is expected to be weak, which allows crustal material to be ductilely shortened and/or Eurasian upper and mid crust to penetrate into the Pamir. B: Schematic sketch showing the geometry of the Pamir intermediate depth seismic zone, figure modified from Sippl et al. (2013). Green and red planes show the locations of the main N-S and the subsidiary NW-SE RF profile, respectively.

Figure 8. Diagonal north-west to south-east cross section using the areal network. In a) the amplitude of the Q-component is migrated assuming horizontal converters. In b) the T-component of the RFs is migrated assuming inclined converters with an inclination angle of 45°. RFs from events with azimuths between 135° and 315° are migrated with reversed amplitudes for the T-component. The data are lowpass filtered with a cut-off period of 3s. This figure is shown without interpretation lines in Fig. S3 in the Supplementary material.

Figure 9. (A-D) Comparison of observed receiver functions and synthetic tests for station P18. Traces are low pass filtered with a cut-off period of 3s. (E-H) Migrated observed QRFs (E) and TRFs (G) and synthetic QRFs (F) and TRFs (H) for station P18. The traces are migrated assuming 50° dipping conversion layers.

Figure 10. Comparison and modeling of waveforms of (A) the Moho (on the Q component) and (B) the slab (on the T component) phases. To match the amplitudes for the LVZ (slab), the velocity contrast at the base of the LVZ has to be chosen to be very similar (97%) to that at the Moho. Amplitudes of the data are normalized to a velocity drop from Vs=4.6 km/s (mantle) to Vs=4.15 km/s (lower crust) at the Moho (Mechie et al., 2012). QRF and TRF data traces used for the modeling are shown in (C) and (D), respectively.

Figure 11. Slant stack results (left column) and receiver functions sorted by slowness (right column) for stations SHAA, FRK9 and IRGN, located in the Tajik basin showing a crustal thickness of ~45 km. On top of each receiver function panel, moveout corrected summation traces for the direct (PS) and multiple phases (PPPS and PPSS) are shown. The theoretical arrival times determined from the slant stack results for the Ps, PpPs and PpSs phases are marked on top by black, yellow and blue lines, respectively.

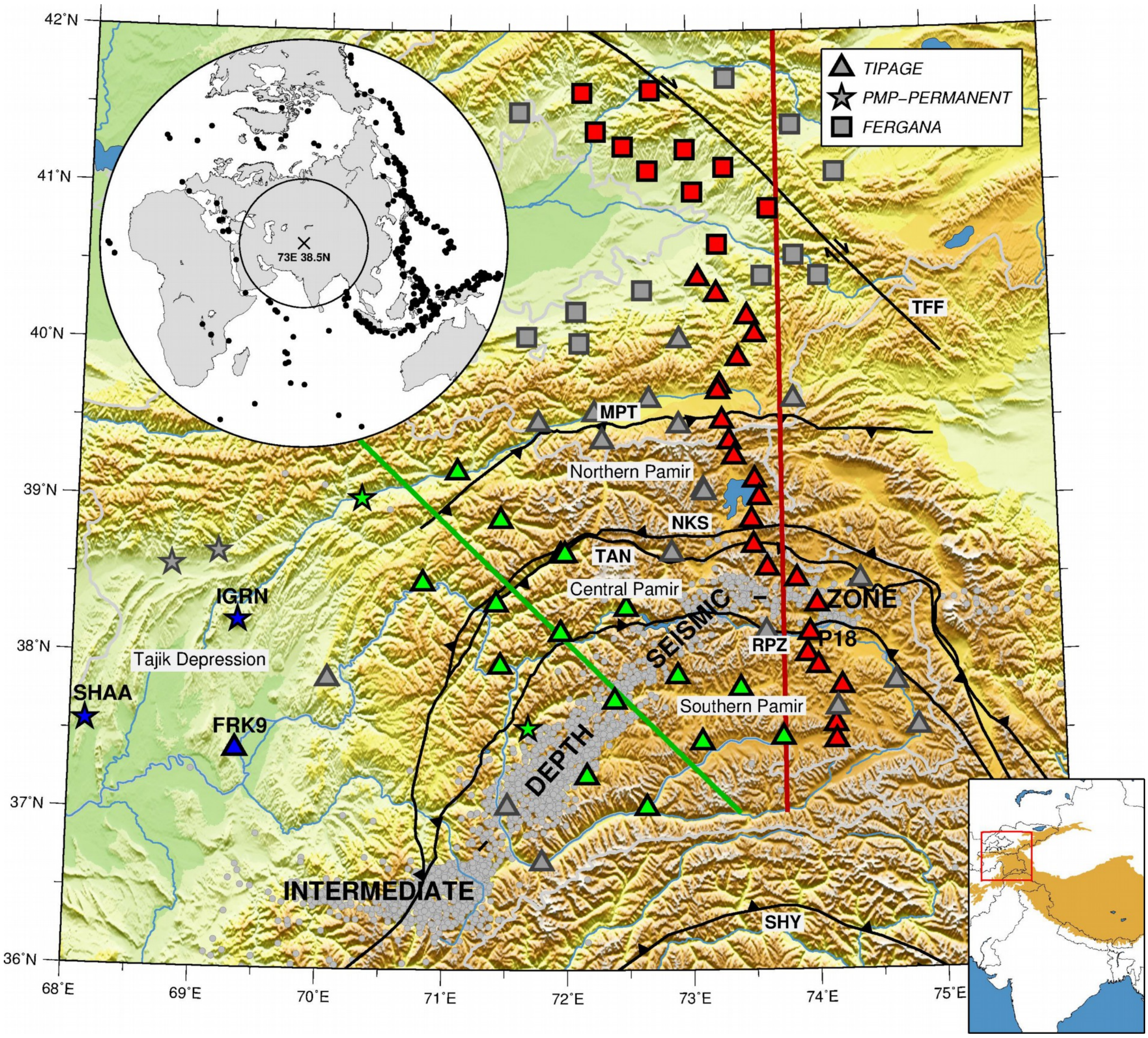

TIPAGE
PMP-PERMANENT
FERGANA
73E 38.5N
TFF
MPT
Northern Pamir
NKS
TAN
Central Pamir
SEISMIC
ZONE
RPZ
P18
DEPTH
INTERMEDIATE
Southern Pamir
SHY
IGRN
Tajik Depression
SHAA
FRK9
42°N
41°N
40°N
39°N
38°N
37°N
36°N
68°E
69°E
70°E
71°E
72°E
73°E
74°E
75°E

Figure 1

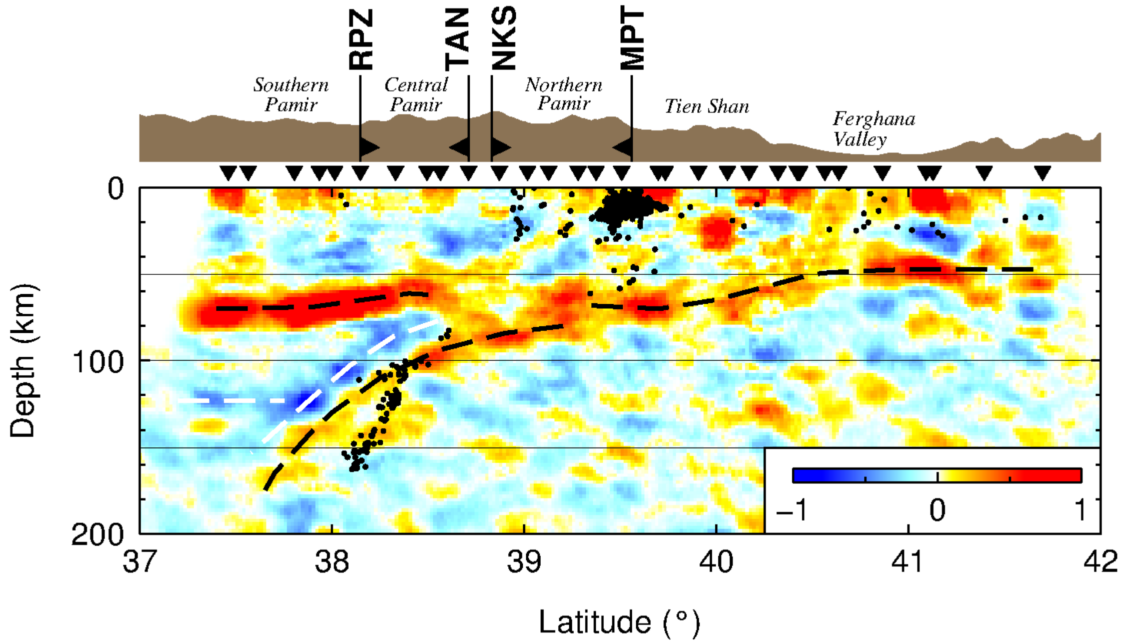
RPZ
TAN
NKS
MPT
Southern Pamir
Central Pamir
Northern Pamir
Tien Shan
Ferghana Valley
Depth (km)
0
100
200
37
38
39
40
41
42
Latitude (°)
–1
0
1

Figure 2

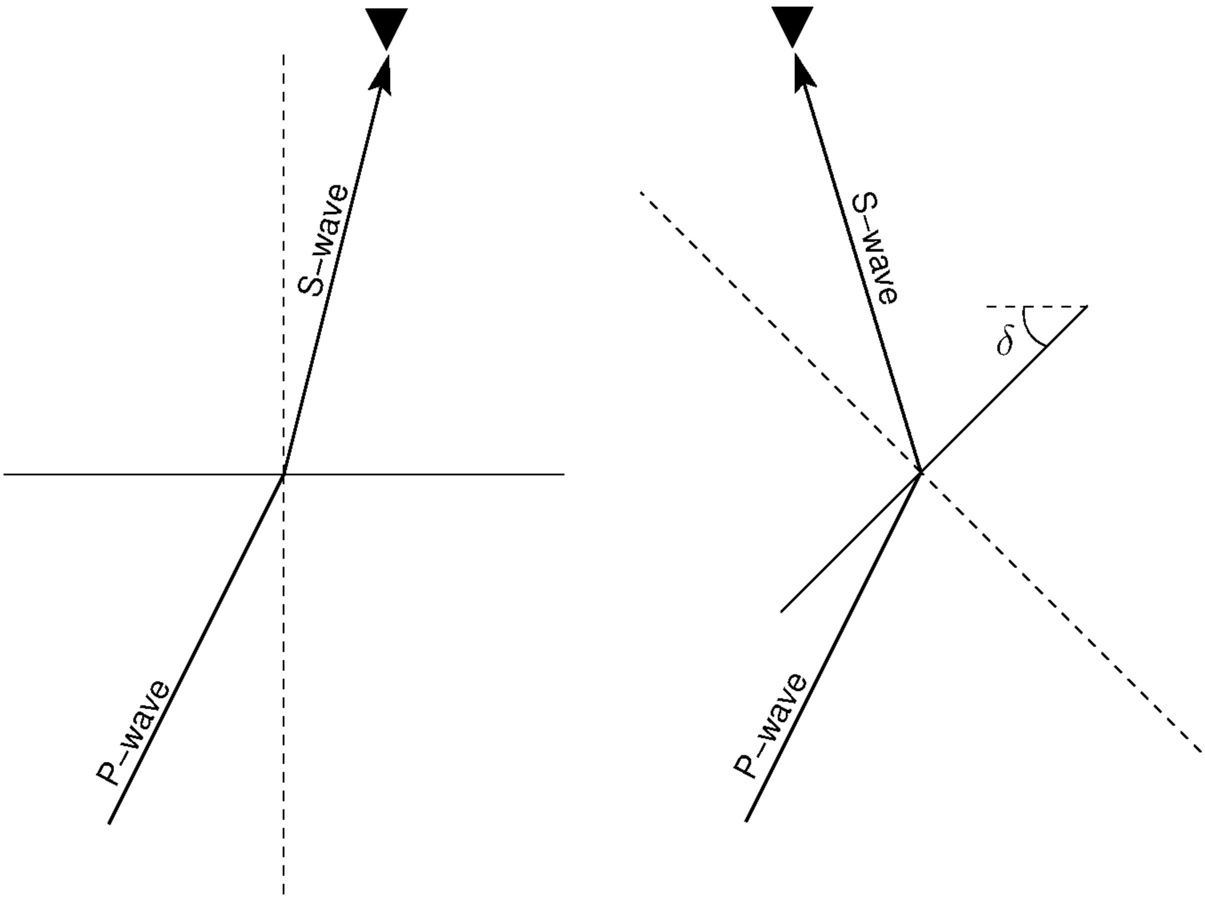

Figure 3

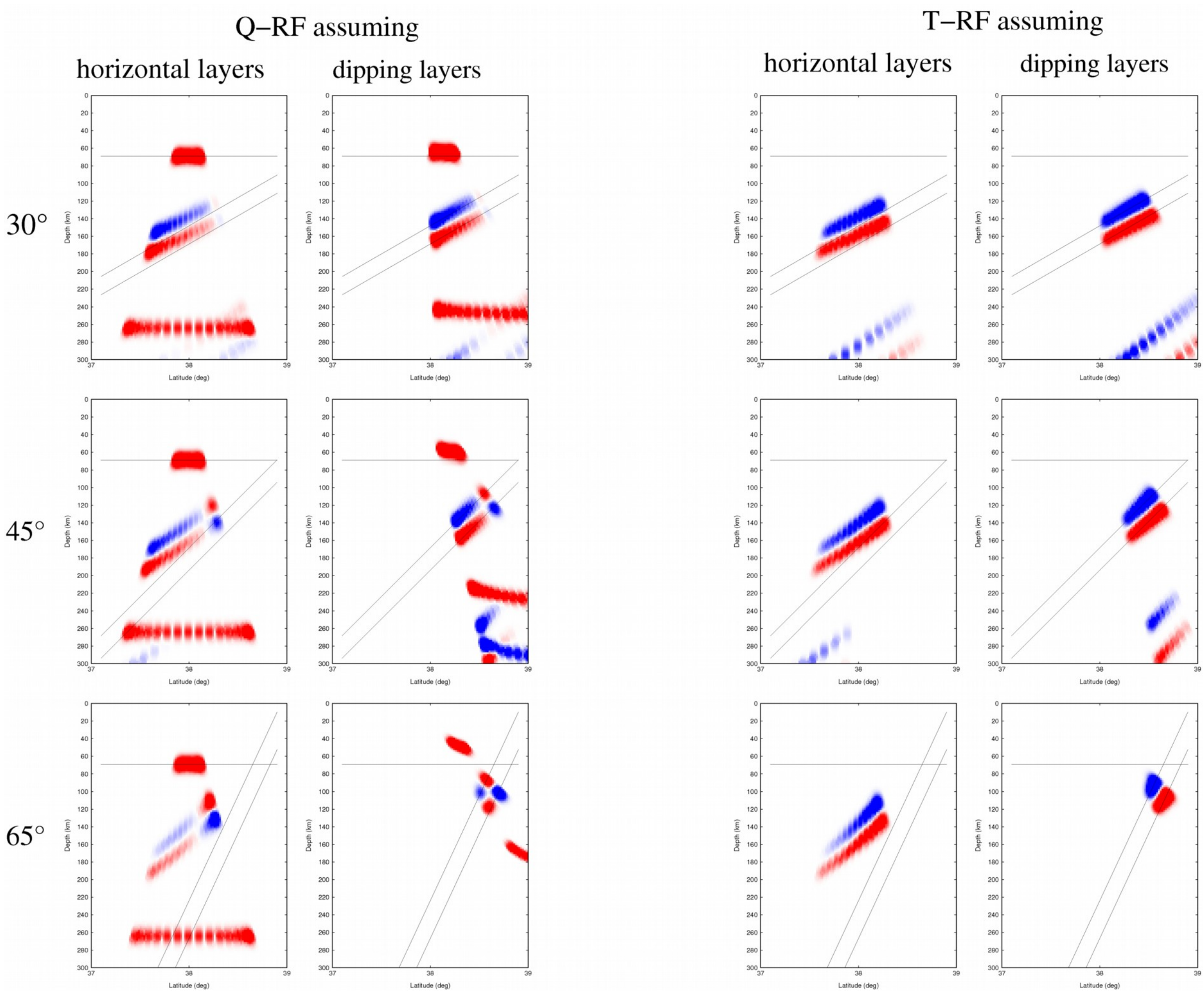

Q–RF assuming
horizontal layers
dipping layers
T–RF assuming
horizontal layers
dipping layers
30°
45°
65°
Depth (km)
Latitude (deg)

Figure 4

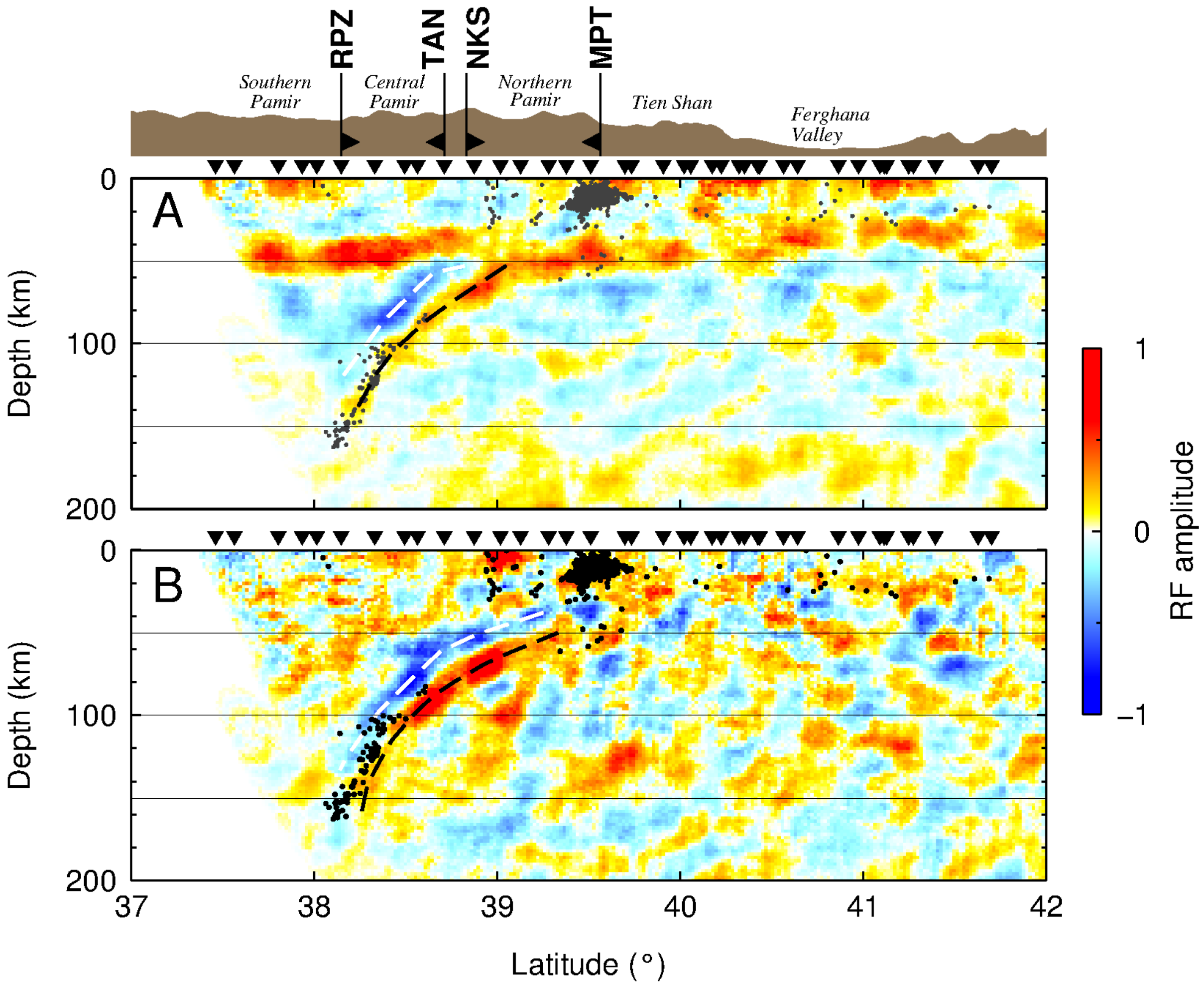
RPZ
TAN
NKS
MPT
Southern Pamir
Central Pamir
Northern Pamir
Tien Shan
Ferghana Valley
A
B
Depth (km)
0
100
200
37
38
39
40
41
42
Latitude (°)
RF amplitude
1
0
−1

Figure 5

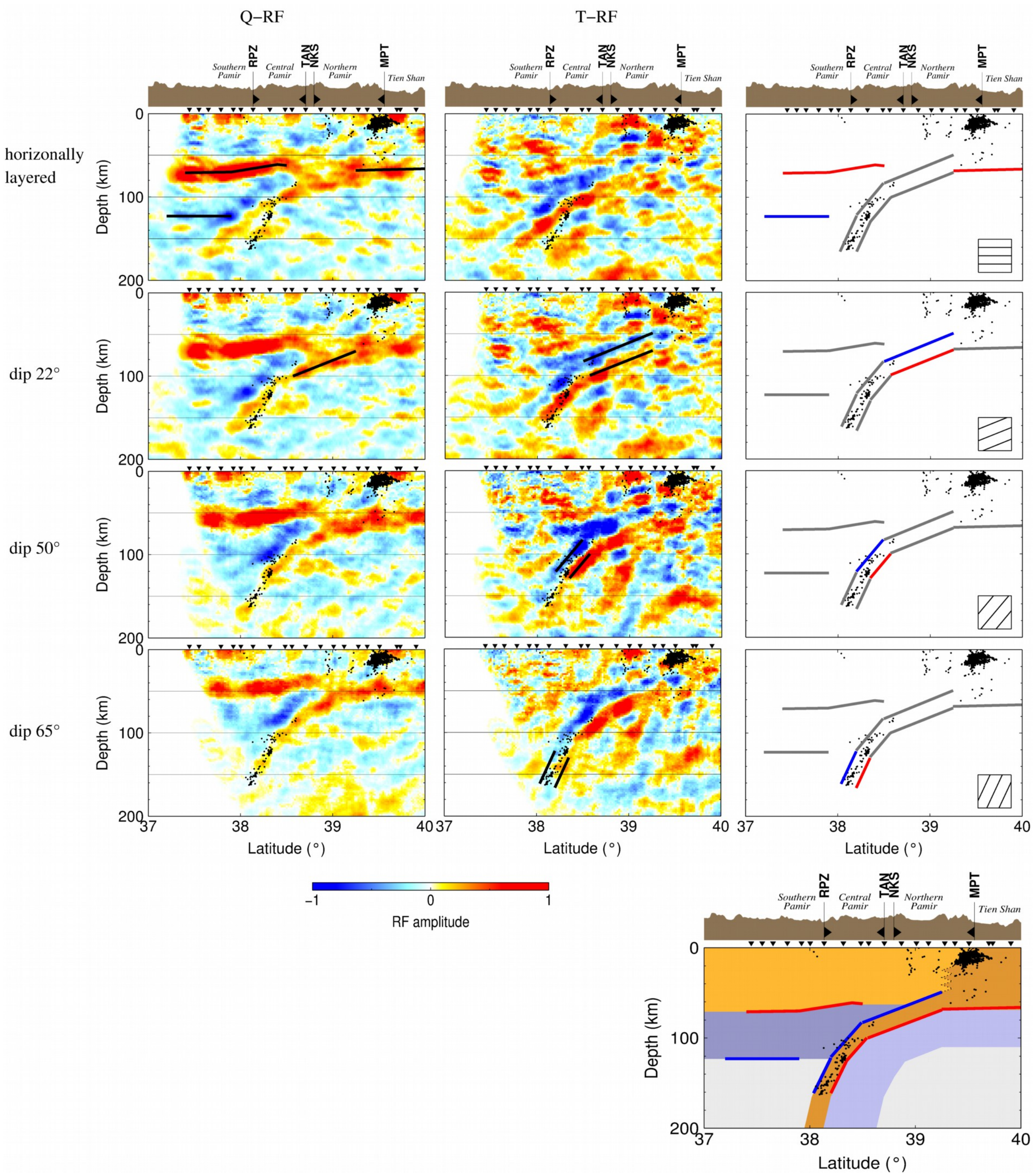
Q–RF
T–RF
horizonally layered
dip 22°
dip 50°
dip 65°
Southern Pamir
Central Pamir
Northern Pamir
Tien Shan
RPZ
TAN
NKS
MPT
Depth (km)
Latitude (°)
RF amplitude

Figure 6

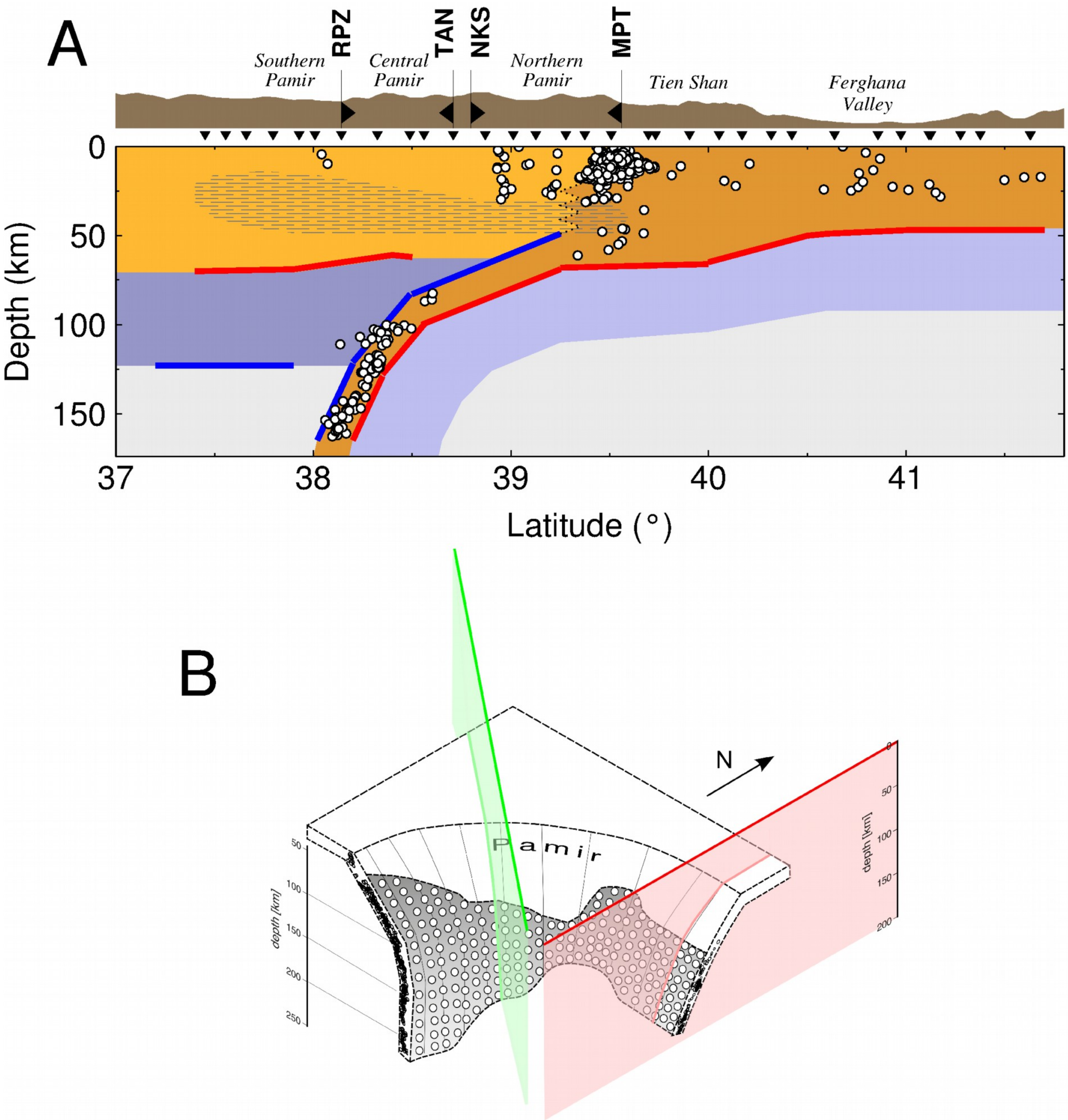

A
RPZ
TAN
NKS
MPT
Southern Pamir
Central Pamir
Northern Pamir
Tien Shan
Ferghana Valley
Depth (km)
0
50
100
150
37
38
39
40
41
Latitude (°)
B
N
Pamir
depth [km]
50
100
150
200
250
0

Figure 7

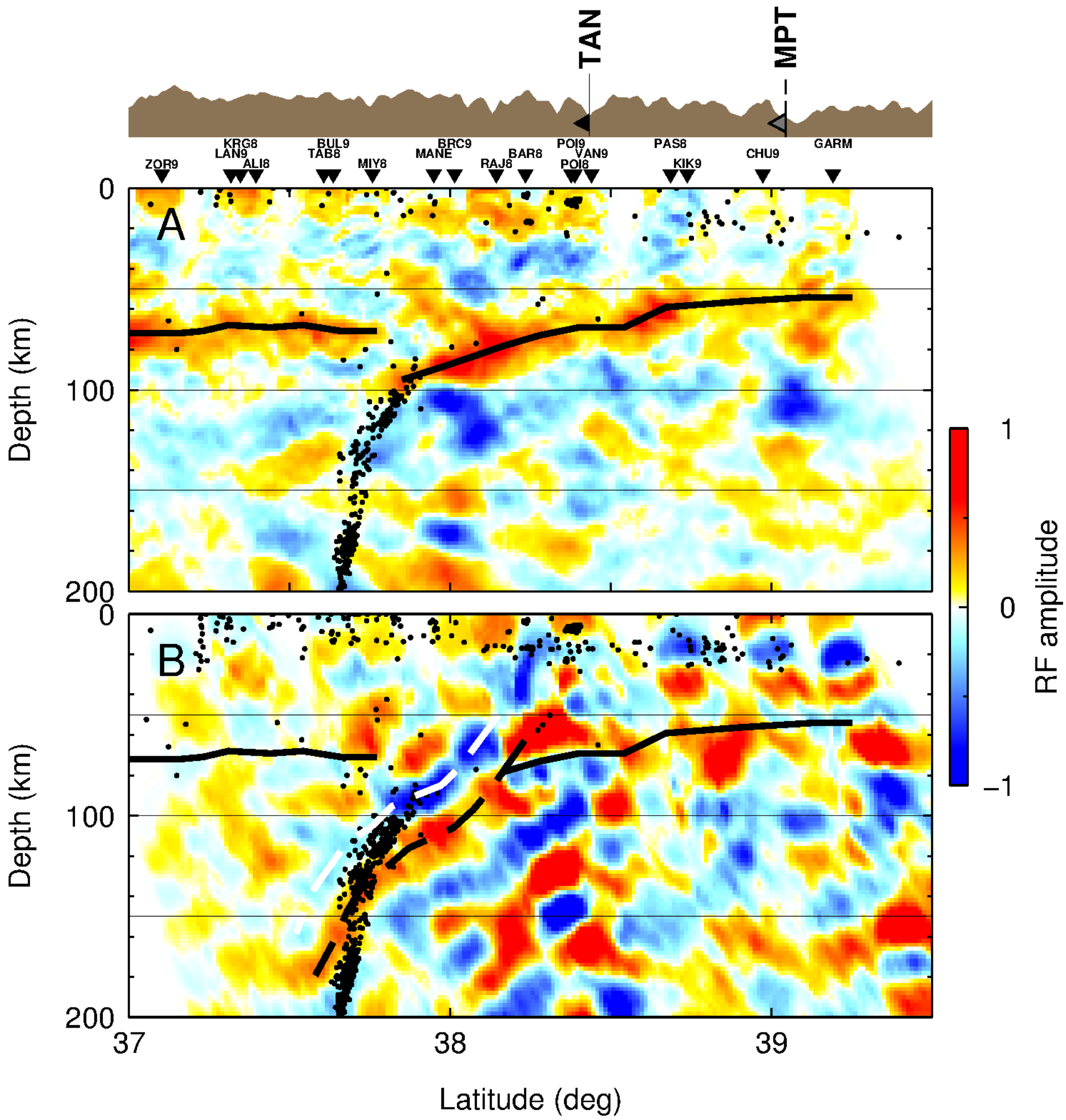
TAN
MPT
ZOR9
KRG8
LAN9
ALI8
BUL9
TAB8
MIY8
MANE
BRC9
RAJ8
BAR8
POI9
VAN9
POI8
PAS8
KIK9
CHU9
GARM
A
B
Depth (km)
Latitude (deg)
RF amplitude

Figure 8

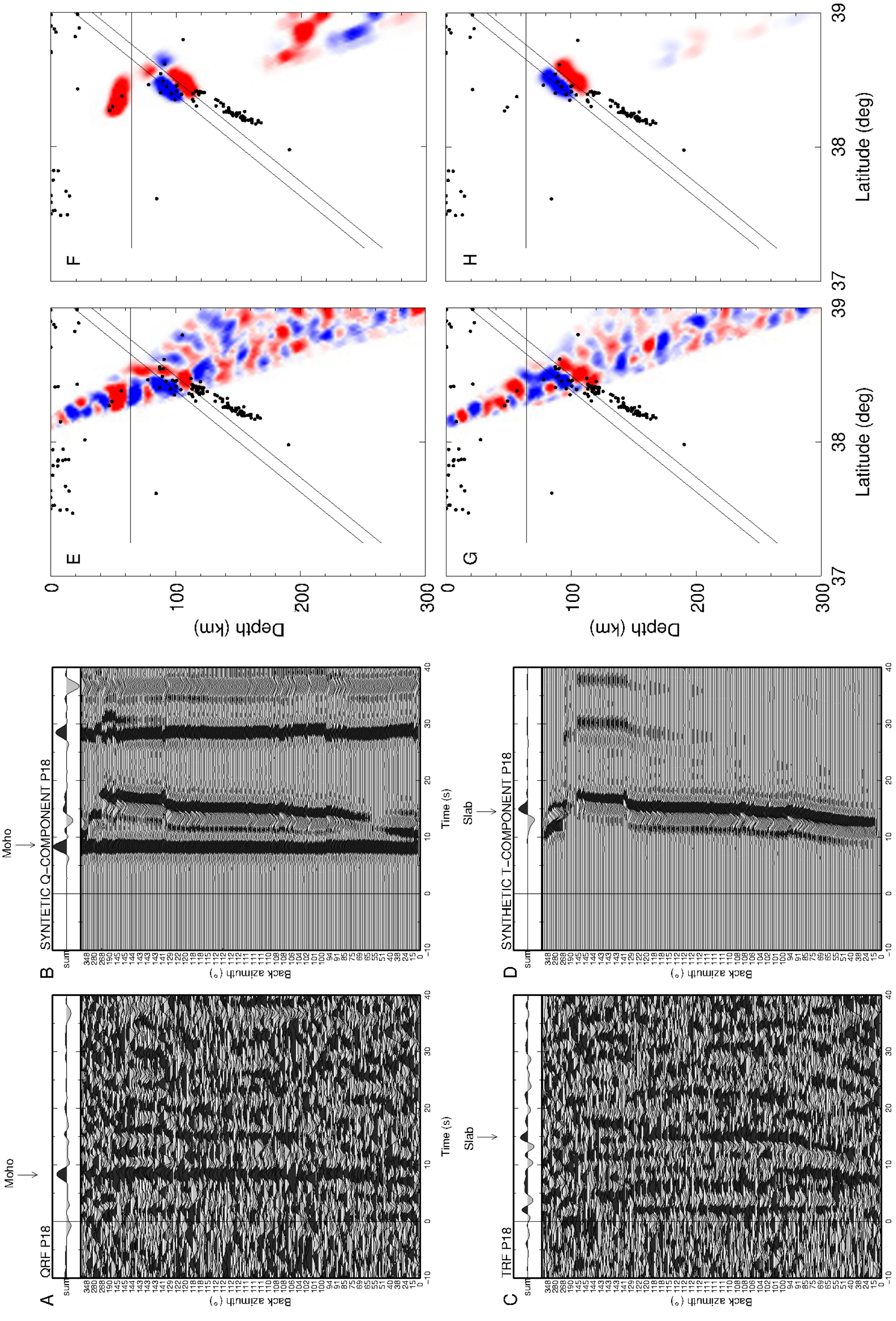

A
QRF P18
Moho
B
SYNTETIC Q-COMPONENT P18
C
TRF P18
Slab
D
SYNTHETIC T-COMPONENT P18
sum
Back azimuth (°)
Time (s)
E
F
G
H
Depth (km)
Latitude (deg)

Figure 9

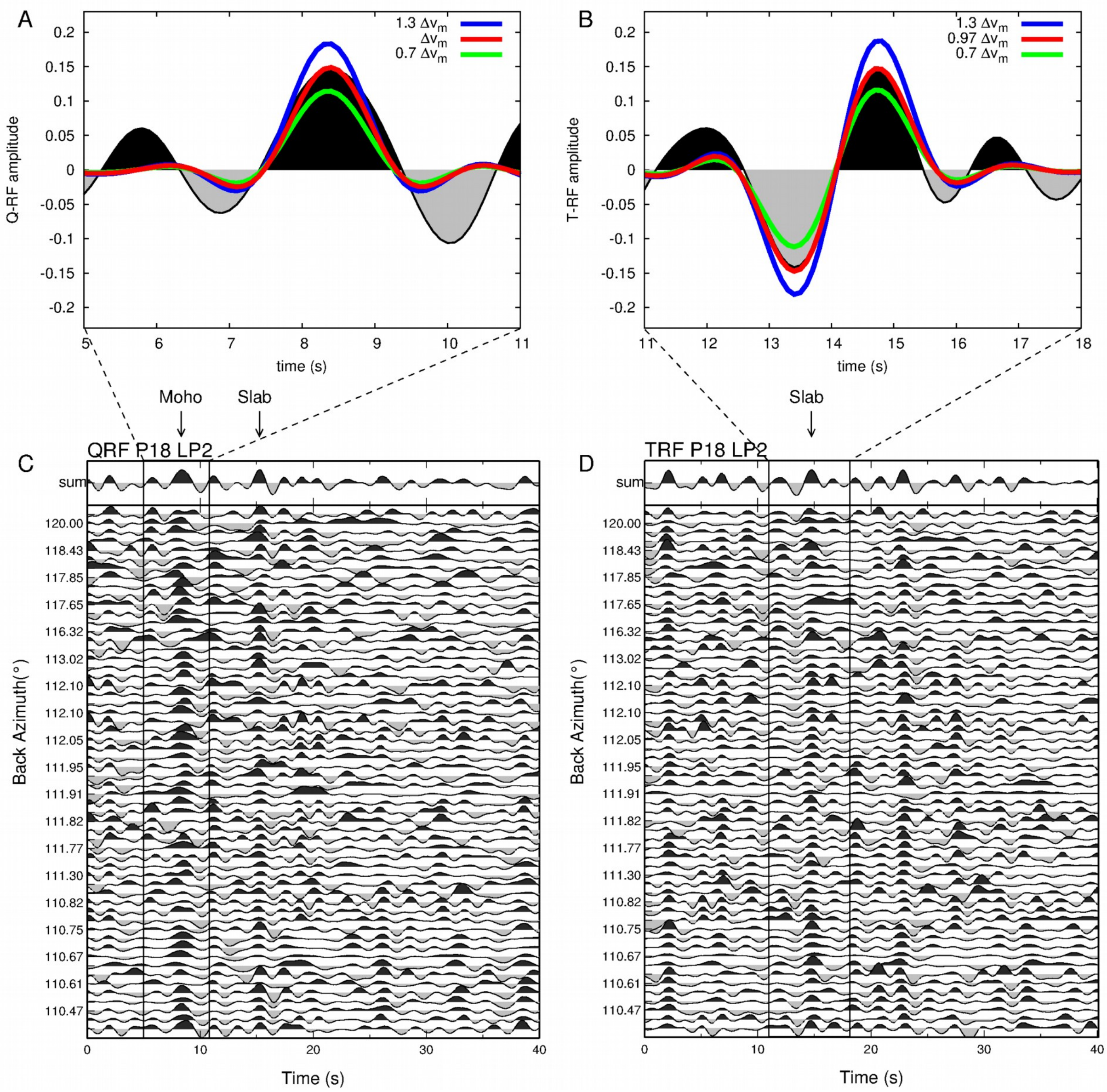

A
B
C
D
1.3 Δv_m
Δv_m
0.7 Δv_m
0.97 Δv_m
Q-RF amplitude
T-RF amplitude
time (s)
Moho
Slab
QRF P18 LP2
TRF P18 LP2
sum
Back Azimuth(°)
Time (s)

Figure 10

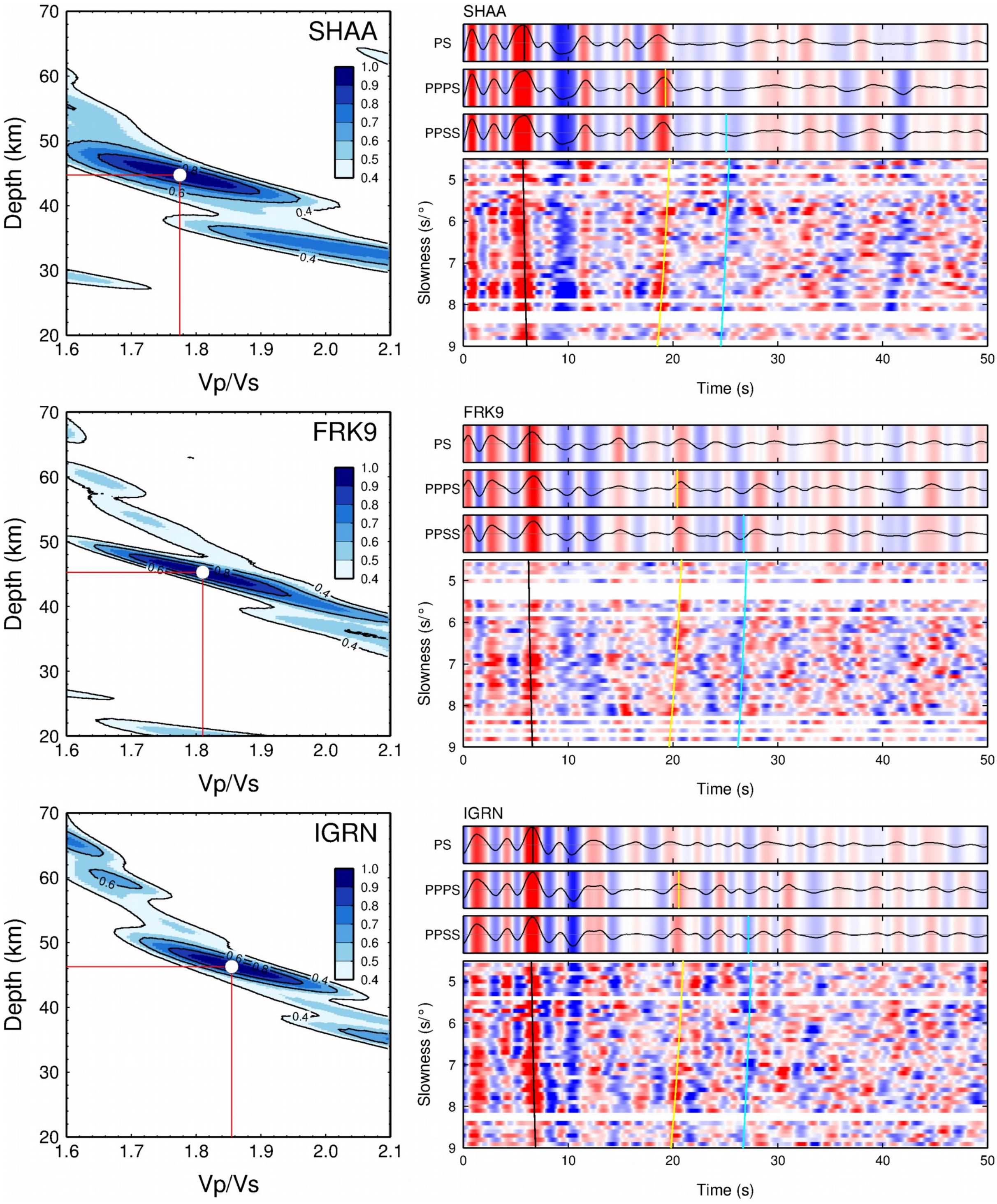

Figure 11

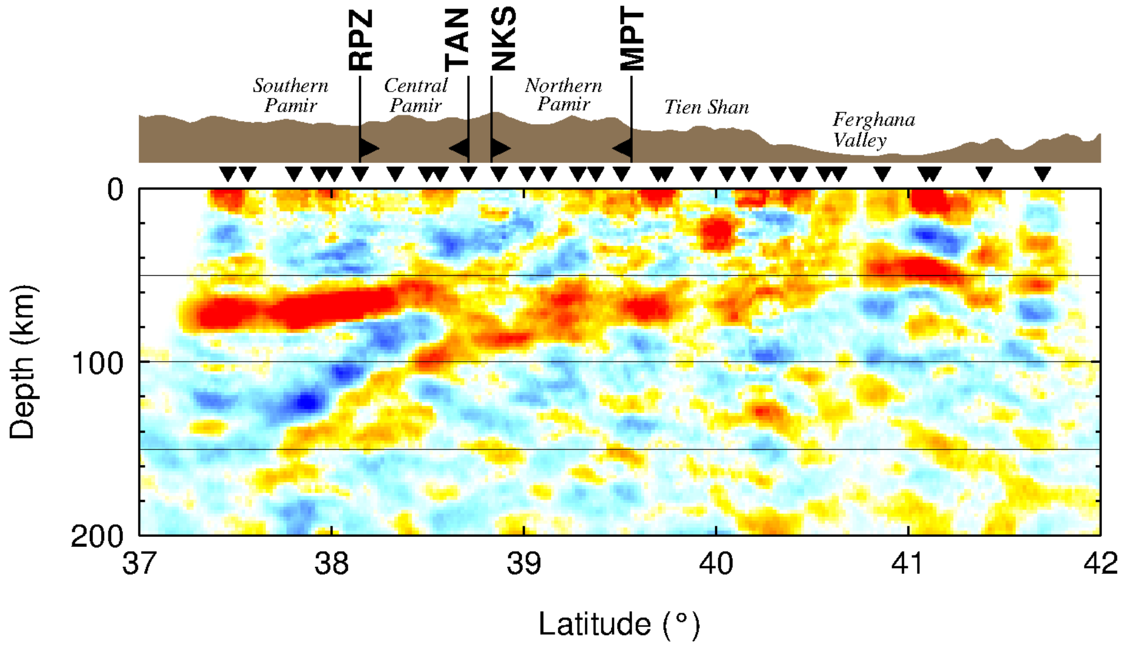

Supplementary Figure S1. Same as Fig. 2 without interpretation lines.

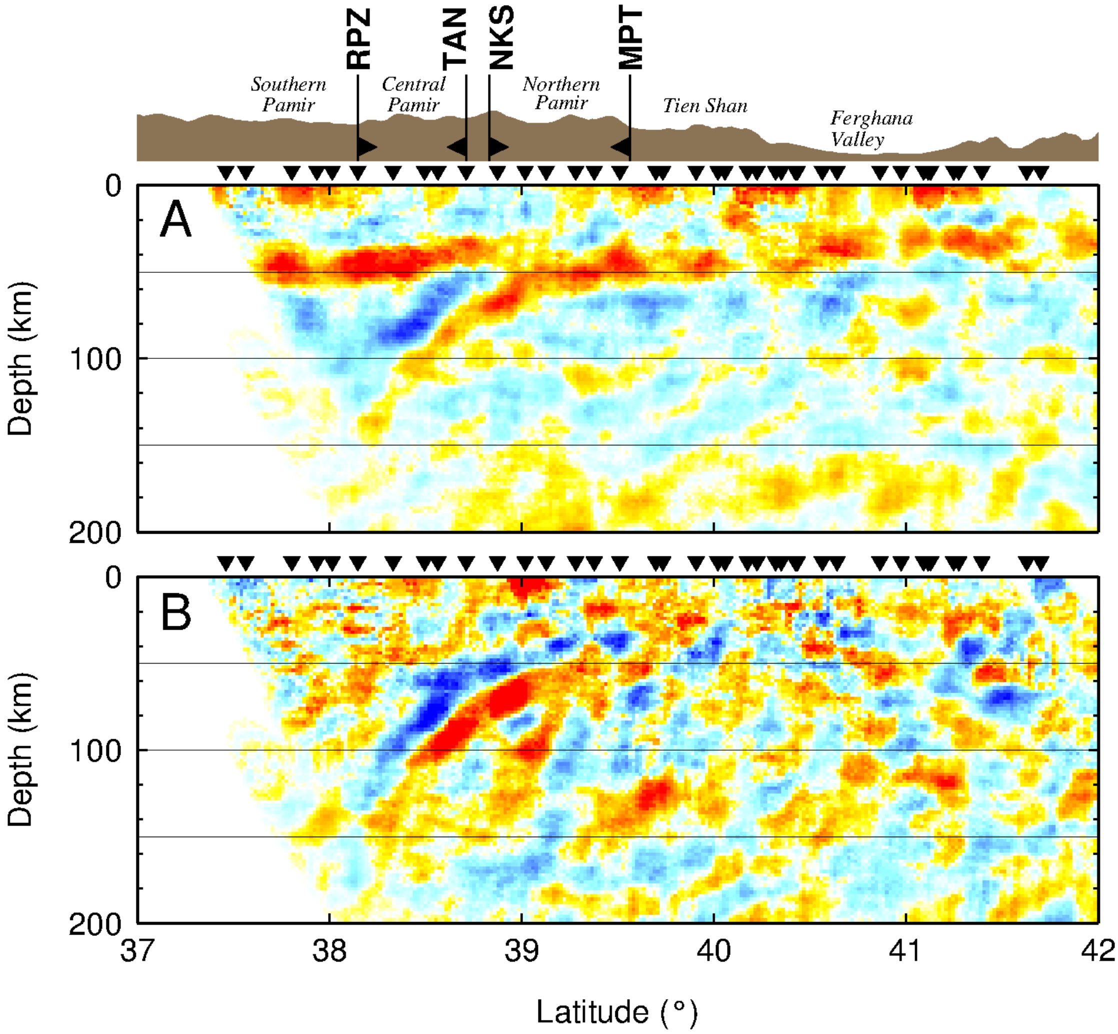

Supplementary Figure S2. Same as Fig. 5 without interpretation lines.

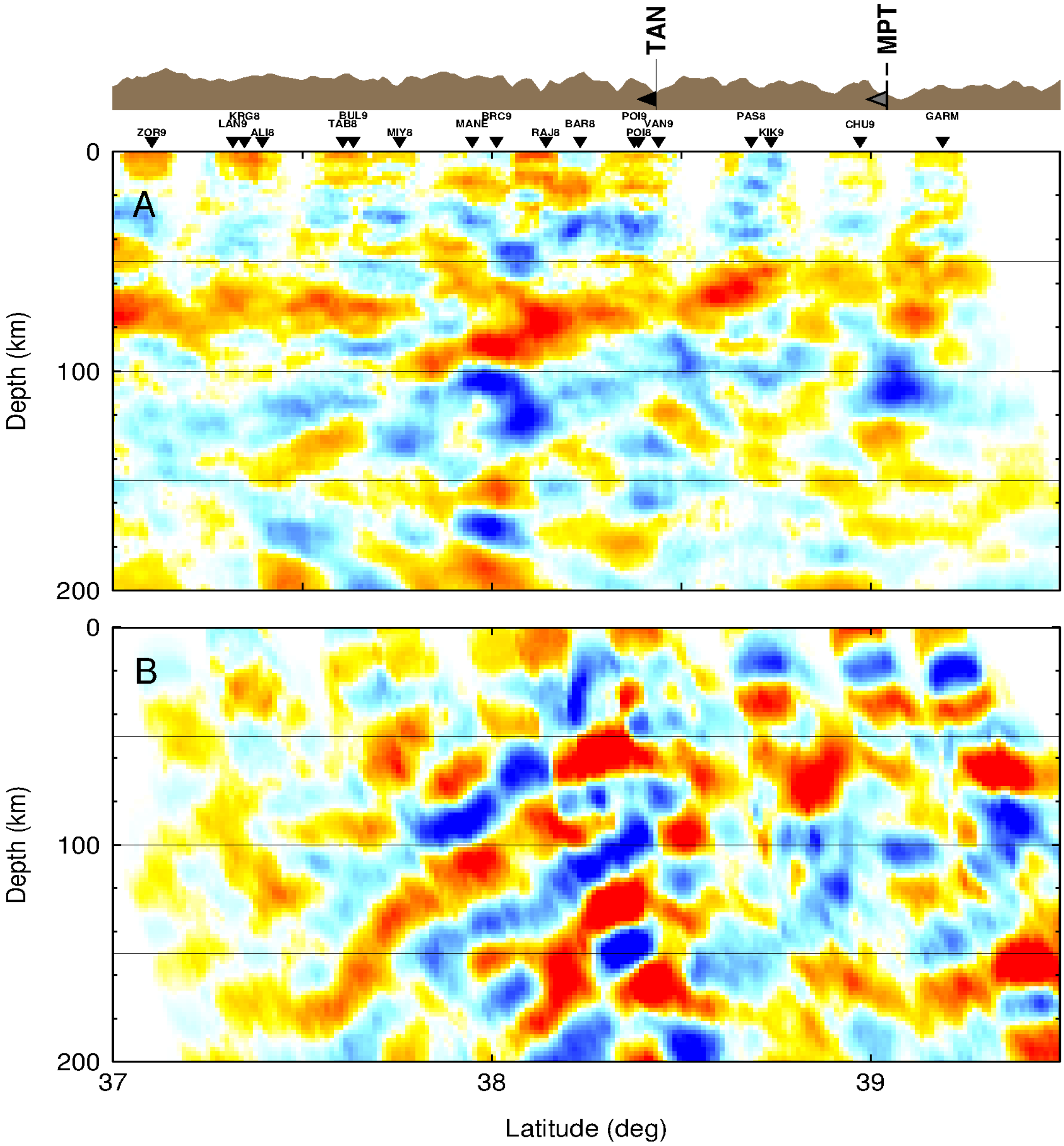

Supplementary Figure S3. Same as Fig. 8 without interpretation lines.

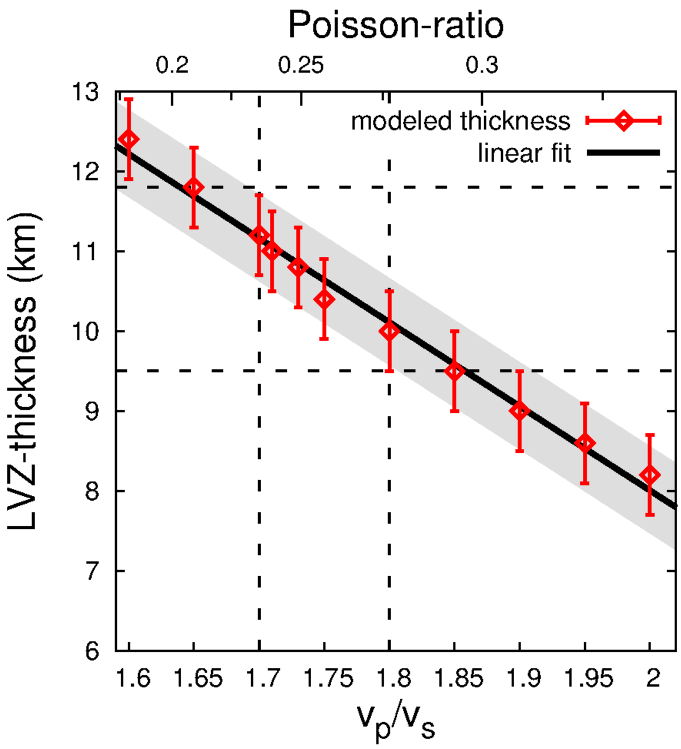

Supplementary Figure S4. Forward modeling of the LVZ phases has been performed for varying Vp/Vs inside the LVZ. A linear dependency between modeled thickness and Vp/Vs is observed. The minimum unit of thickness difference that can be distinguished visually by comparing the synthetic TRFs with the data is 0.5 km, which is thus given as the error for each model. In the Vp/Vs interval from 1.7 to 1.8 the LVZ thickness ranges between 9.5 and 11.8 km.

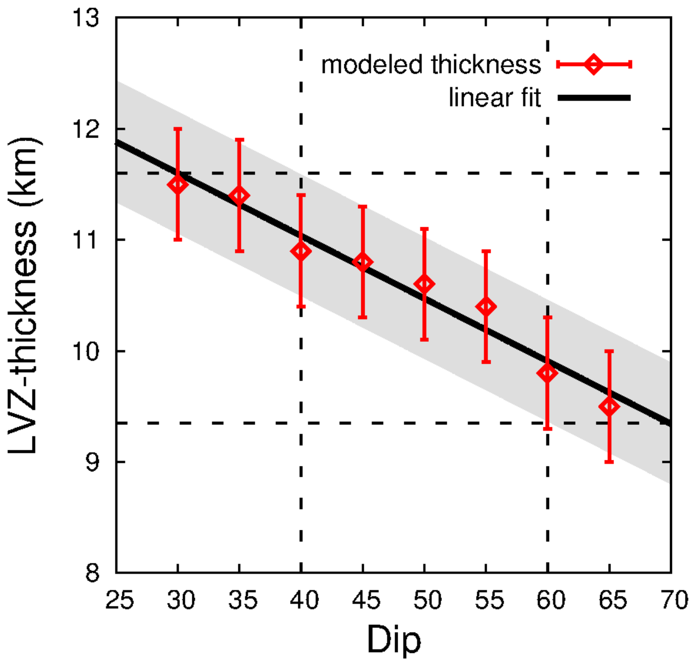

Supplementary Figure S5. Forward modeling of the LVZ phases has been performed for varying inclination angle (dip) of the LVZ. In the forward modeling process, the minimum thickness difference that can be distinguished visually by comparing synthetic and observed TRFs is 0.5 km, which is thus given as the error for each modeling. Assuming a dip of 50° +/- 10° the LVZ thickness can be estimated to be 10.5 +/- 1 km.

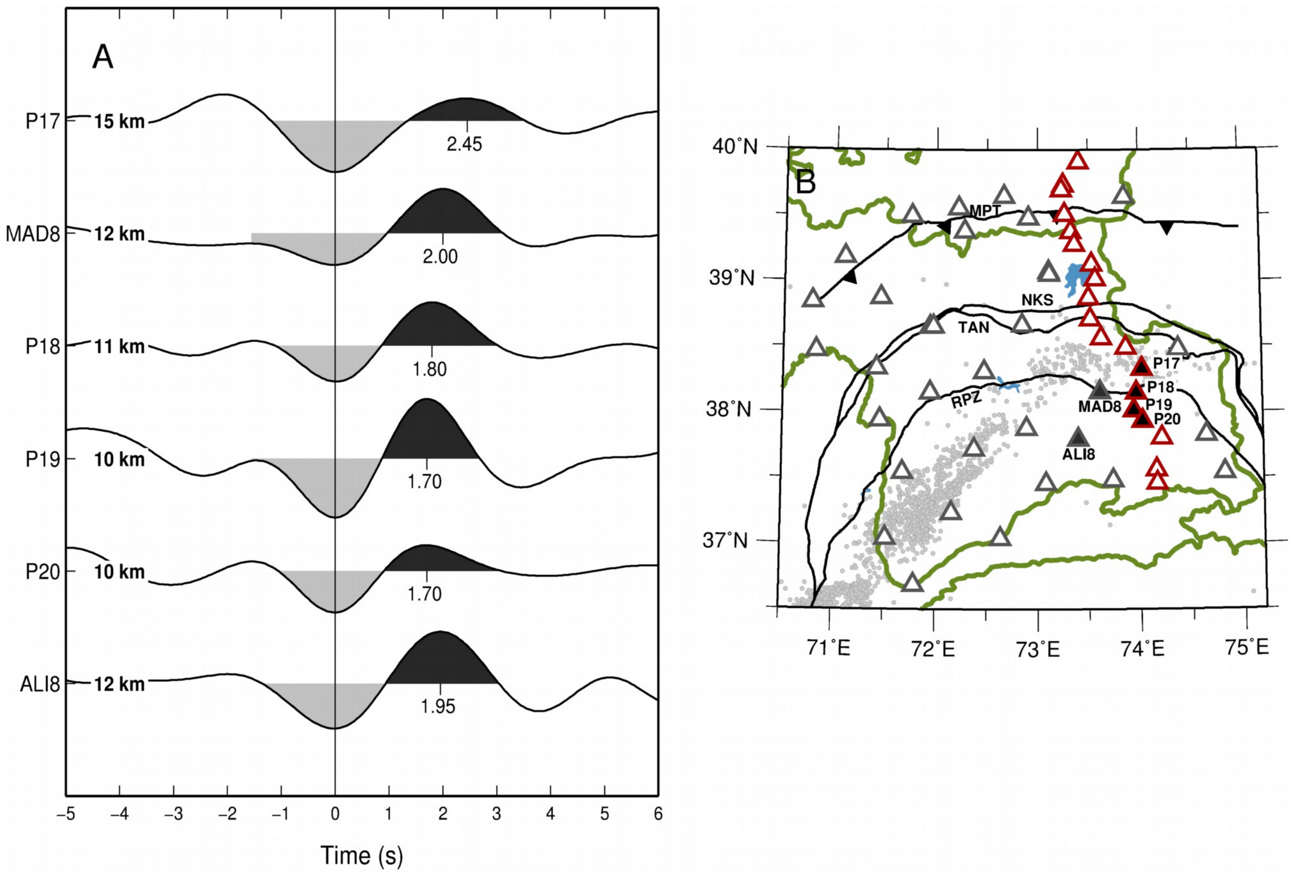

Supplementary Figure S6. A: The TRF conversion phases of the LVZ at 6 stations as seen in a back azimuth range from 30° to 110°. For each station the leading negative phases were aligned at 0 s and stacked. The delay time between negative and positive conversions and corresponds to the thickness of the LVZ. Starting with the forward modeling at station P18, the thicknesses of the LVZ at the different stations were linearly extrapolated, taking into account the delay times at each station relative to the delay time at station P18. The resulting thicknesses are given at the left side of each trace. In this way, the LVZ thickness is estimated to be 10-15 km. B: Station map showing the positions of stations P17, MAD8, P18, P19, P20 and ALI8 as black filled triangles. Stations of the N-S profile are depicted as red triangles, the other stations of our network as gray triangles.

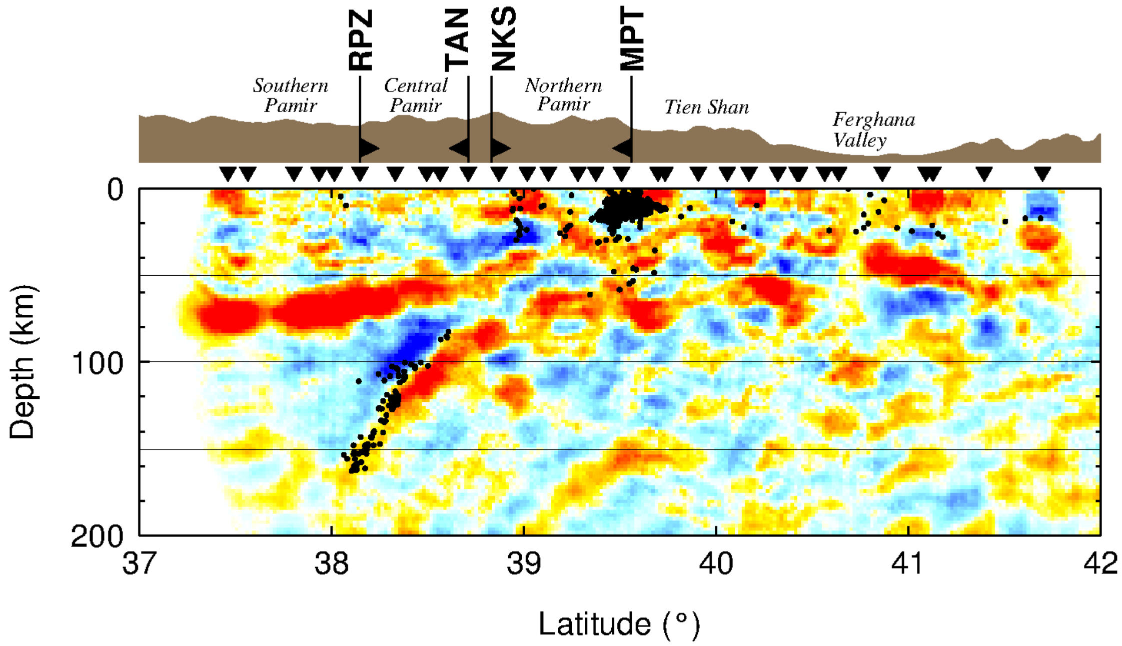

Supplementary Figure S7. Common conversion point (CCP) image along the N-S main profile with QRF and TRF components stacked together in each grid cell. For depths greater than 80 km CCP stacking was performed for 50° inclined conversion interfaces to image the LVZ, while for shallower depths horizontally layered converters were assumed to image the Moho at the right depth. The same processing on the CCP stacked data was applied as in Fig.2. Key: see Fig. 1.

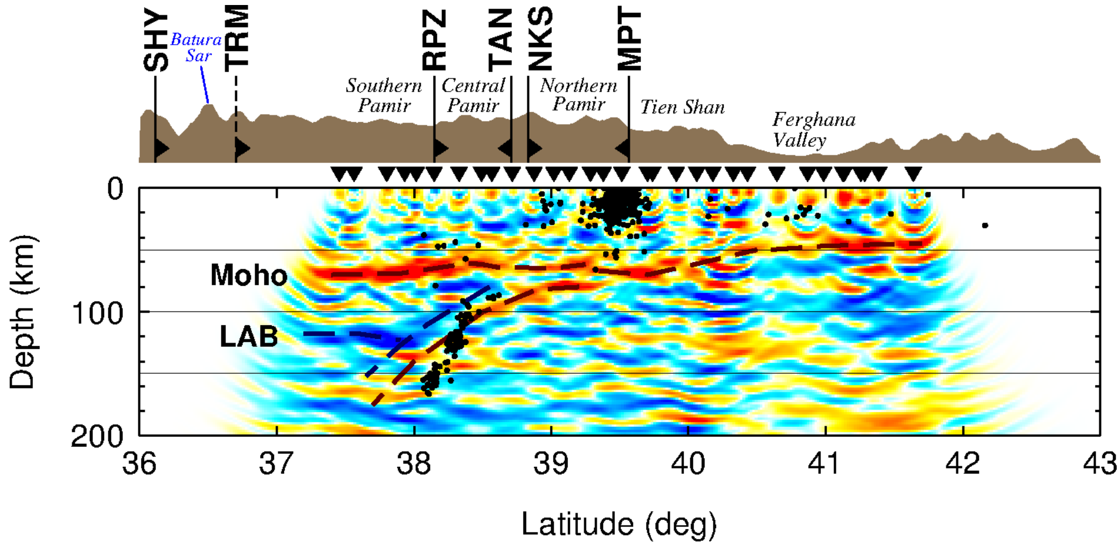

Supplementary Figure S8. Depth section of QRFs along the main N-S profile converted to depth using a Fresnel-zone stacking algorithm. After the stacking a boxcar filter with 6 km diameter was applied. This image shows a clear negative signal south of the subducting LVZ labeled as the lithosphere-asthenosphere boundary (LAB). Key: see Fig. 1.